A Study of Warm Absorbers in Active Galactic Nuclei

Ceri Ellen Ashton

Mullard Space Science Laboratory
Department of Space and Climate Physics
University College London

A thesis submitted to the University of London
for the degree of Master of Philosophy

October 2005

Abstract

This thesis explores the 'warm absorber' phenomenon observed in Active Galactic Nuclei (AGN). Warm absorbers are clouds of ionised gas within AGN, that cause absorption at soft X-ray wavelengths. They are observed in half of all Type 1 AGN, hence they play an important part in the framework of our understanding of Active Galactic Nuclei. Observations with the satellite *XMM-Newton* have given us the highest signal-to-noise data yet.

XMM-Newton observations of the quasars PG 1114+445 and PG 1309+355 are studied. Both quasars exhibit evidence for absorption by warm material in the line-of-sight. We define a 'phase' of absorption to have a single ionisation parameter and column density. From fits to the data, the absorption in PG 1114+445 is found to be in two phases, a 'hot' phase with a log ionisation parameter ξ of 2.57 and a column of 10^{22} cm^{-2}, and a 'cooler' one with log ξ of 0.83 and a column of 10^{21} cm^{-2}. The absorption in PG 1309+355 consists of a single phase, with log ξ of 1.87 and a column of 10^{21} cm^{-2}. The absorbing gas lies at distances of 10^{19} - 10^{22} cm from the continuum radiation sources in these AGN, suggesting origins in a wind emanating from a molecular torus, according to the 'Standard Model' of AGN. The kinetic luminosities of the outflowing absorbers represent insignificant fractions ($< 10^{-3}$) of the energy budgets of the AGN.

Using data for the Seyfert 1 H 0557−385, the warm absorption is characterised by two phases, a phase with log ξ of 0.48 and a column of 10^{21} cm^{-2}, and a phase with log ξ of 1.63 and a column of 10^{22} cm^{-2}. Neutral absorption is also present in the source, and possible origins for this are discussed.

For a large sample, observations of warm absorbers are collated and compared with models.

Contents

List of Figures

List of Tables

Acknowledgements

There are many people whom I have consulted for help during the writing of this thesis; I'm sure you know who you all are!

My greatest thanks goes to my supervisors, Graziella Branduardi-Raymont and Mat Page, for their guidance, help and the great amount of time they have devoted to me, during my time at MSSL. It has been a pleasure to know such marvellous people. I have benefited greatly from Graziella's vast stores of knowledge, and also her perfect command of the English languge which has shamed my own schoolgirl grammar on many occasions. Similarly I have learnt much from the huge amounts of time and effort Mat has devoted to me; I believe his sarcasm has done me no lasting damage, and I hope sincerely he will discover there are more culinary delights to be had than pot noodles.

I have also taken up a great deal of time from Alex Blustin and Rhaana Starling, whom I thank deeply for their help and friendship. Thanks also to Catherine Brocksopp, Nicola Loaring, Gavin Ramsay and Roberto Soria for being great friends and colleagues.

I am pleased to have made the friendship of so many great people in the church and village of Holmbury St.Mary, a definitive quintessential English village; their interest in the work of MSSL has been inspiring. I also owe a great deal to Mumsy, and her alarming ability to predict the future, generally quite useful but especially so in times of crisis. I thank the Rev. Pam Robson for being a great mentor, and Anne Payne, Annika Lohstroh and David Folkerd for their support in finishing the thesis.

I would also like to thank Stephen Coulson and his family for their immense hospitality towards me during my first year in Surrey (and in England, for that matter.)

I am grateful to PPARC for financial support for the last 3 years.

I acknowledge initial guidance from the late Liz Puchnarewicz, an enthusiastic astronomer who introduced me to PG quasars and, amongst other things, refined my soul with fire. I doubt I will meet her like again.

Diolch yn fawr a iechyd da!

This work is based on observations obtained with XMM-Newton, an ESA science mission with instruments and contributions directly funded by ESA Member States and the USA (NASA). This research has made use of the NASA/IPAC Extragalactic Database (NED) which is operated by the Jet Propulsion Laboratory, California Institute of Technology, under contract with the National Aeronautics and Space Administration. This research has also made use of the SIMBAD database, operated at CDS, Strasbourg, France.

The copyright of this thesis rests with the author and no quotation from it or information derived from it may be published without the prior written consent of the author.

When I consider thy heavens,

the work of thy fingers,

the moon and the stars, which thou hast

ordained;

What is man, that thou art mindful of him?

And the son of man, that thou visitest him?

Psalm 8

Chapter 1

Introduction

1.1 Discovery of AGN

AGN have fascinated astronomers for about a century now. But what are the historical milestones that have led to the discovery of this most powerful class of galaxies?

The first optical spectrum of an AGN was taken of NGC 1068 in 1908 (Fath 1909). Even then, emission lines were noted in the spectrum. Very soon after, a higher-quality spectrum showed that the lines are resolved and have widths of hundreds of km s^{-1}. In 1926, in a study of extragalactic nebulae, Edwin Hubble noted strong emission-line spectra of three galaxies: NGC 1068, NGC 4051 and NGC 4151 (Hubble 1926). In 1943, Carl Seyfert was the first to identify a class of spiral galaxies with bright, compact nuclei. Seyfert found that the optical spectra of these bright galaxies have strong nuclear emission lines, and these are now known as Seyfert galaxies.

In the 1960s, the apparent 'stars' 3C 273 and 3C 64, both strong radio emitters, were measured to be at the then-huge redshifts of 0.158 and 0.367 respectively. Dubbed quasi-stellar radio sources, later shortened to quasars, it was realised that sources of this type all have large redshifts, broad emission lines and

are variable.

Astronomers have tried to account for the different properties of AGN by invoking a unified model that can explain them all. First I describe the properties of AGN, then I review the classes of AGN that have been identified.

1.2 What is an AGN?

Astronomers believe that at the centres of AGN there reside supermassive black holes, with masses of millions of solar masses. They are immensely powerful, capable of generating huge amounts of energy ($> 10^{47}$ erg s^{-1}), and they emit radiation across practically the whole electromagnetic spectrum.

In the 1960s, the huge distances that quasars are at was first realised, implying that they must have very high luminosities. It was suggested that such luminosities could be produced by the efficient conversion of gravitational potential energy released by gases falling onto a black hole, into radiation by friction in the accretion disk (e.g. Lynden-Bell 1969). Friction in the disk causes it to become very hot ($\sim 10^5$-10^6 K) to the extent that it emits large amounts of X-rays. Other effects are relativistic jets, boosted out along the disk's axis.

Black holes can be spinning or not; spinning black holes are called Kerr black holes, and non-spinning black holes are called Schwarzschild black holes. The radius of the last stable orbit before material is sucked into a Kerr black hole is $2GM/c^2$, where G is the gravitational constant, M is the black hole mass and c is the speed of light. For a Schwarzschild black hole the last stable orbit has a radius equal to $6GM/c^2$.

The physical structure of AGN is now quite well understood. Starting at the centre and moving out, we have the black hole, and the hot accretion disk, which is of scales of light days. Then we have the broad-line region (BLR) clouds, on scales of hundreds of light days. The BLR clouds are whirling around rapidly as they are quite close in to the AGN, and yield optical emission lines with widths

of thousands of km s^{-1}. They also have high densities, with electron densities 10^9 cm^{-3} or higher. Further out is the torus. This is an optically thick doughnut-shaped ring of cold gas and dust that surrounds the central source, and is scales of parsecs across. The narrow-line region (NLR) clouds, on scales of hundreds of parsecs, are much further from the AGN and so do not whirl round quite as fast as those of the BLR; the NLR optical emission lines have widths of hundreds of km s^{-1}, and can be resolved. The NLR clouds are low-density ionised gas (electron densities 10^3-10^6 cm^{-3}).

Lastly we have radio jets, which can extend to Mpc scales. Jets of relativistic particles and magnetic fields are responsible for the radio emission: this is thought to be due to synchrotron radiation of high energy electrons spiralling along magnetic fields. Whether an AGN is radio-loud or radio-quiet is defined by the strength of the jet radio emission, if present at all. Fanaroff & Riley (1974) found that extended radio structures can be divided into two separate luminosity classes.

Images of the torus and radio jet in the galaxy NGC 4261 are shown in Fig. 1.1.

1.3 Classes of AGN

The classification of AGN according to their observational properties has evolved throughout the decades, as better instrumentation has become available and features could be resolved to a higher degree.

The two types of AGN studied in this thesis are quasars and Seyfert galaxies. First discovered optically (Seyfert 1943), Seyferts can be classified as either type 1 or type 2, depending on the widths of their optical emission lines: some AGN were seen to have optical emission lines with widths up to thousands of km s^{-1} (Seyfert 1s) whereas others have widths of only hundreds of km s^{-1} (Seyfert 2s).

These days, the term 'quasar' refers to both radio-loud and radio-quiet sources, although only $\sim$ 10 % of quasars are radio-loud.

Another class of AGN is BL Lacs. Greatly studied in the 1960's and 1970's, a characteristic of these objects is the absence of strong absorption or emission lines in their spectra. They are also polarised, variable and radio-loud; they are thought to be radio galaxies with the radio jets viewed pole-on.

The reason for the dichotomy between Seyfert 1s and Seyfert 2s is explained by the 'Unified Model' for AGN (Antonucci 1993; see Fig. 1.2). The dichotomy is believed to arise from the obscuration of the central continuum source by the torus, an optically thick doughnut-shaped ring of cold gas and dust that surrounds the central source. Crucial evidence for the Unified model was found by Antonucci & Miller (1985), who discovered a hidden Seyfert 1 nucleus in the Seyfert 2 NGC 1068, by polarisation measurements of continuum and broad line photons, scattered by electrons that lie above the torus. If we are looking directly at the central source, then no obscuration is present and we will observe both the broad and narrow line regions (Seyfert 1s); if we are looking through the torus, then we will only observe the narrow line region (NLR) clouds which lie outside the torus, and the broad line region (BLR) will be obscured (Seyfert 2s). As mentioned earlier, the BLR clouds are close to the AGN, their optical emission lines have widths of thousands of km s^{-1} and are produced at high densities (electron densities 10^9 cm^{-3} or higher). The NLR clouds are much further from the AGN, and have line widths of hundreds of km s^{-1}. They consist of low-density ionised gas (electron densities 10^3-10^6 cm^{-3}). The NLR is shaped by the torus into 'ionisation cones', and the shape can be discerned in Seyfert 2 AGN as they are observed from the side (e.g. Capetti et al 1999). The best example of ionisation cones is seen in NGC 1068 (Pogge 1988). A range of intermediate types between Seyfert 1s and 2s also exist, dependent on the ratio of the broad to narrow line strength. Maiolino & Rieke (1995) find that Seyfert 2s are 4 times more numerous than Seyfert 1s.

Fig. 1.2 shows what is currently believed to be the AGN model that explains the many different observed types.

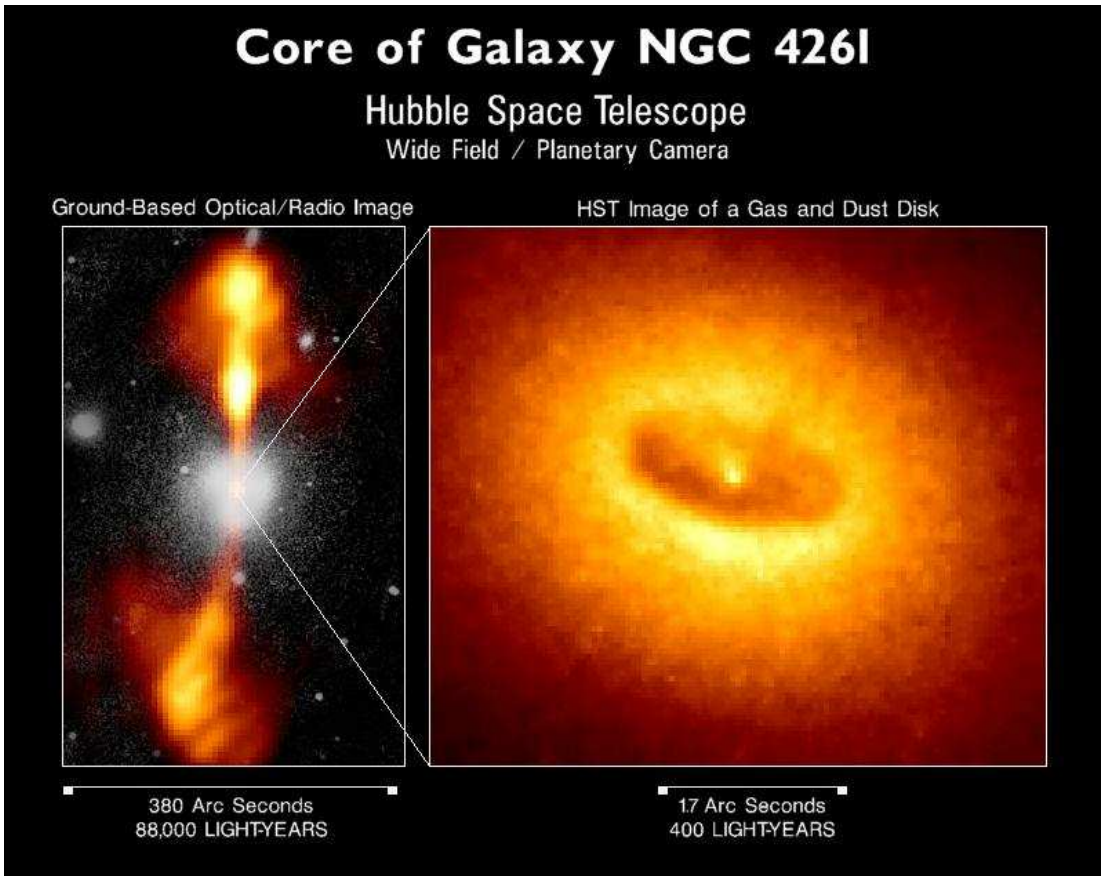

Figure 1.1: Images of the galaxy NGC 4261. LHS: an optical image (white) is superimposed on a radio image (orange). The central source and radio jets are very clear. RHS: a close-up of the central source reveals the gas and dust torus. Credit for figure: http://hubblesite.org/newscenter/newsdesk/archive/releases/1992/27/image/b

The most important difference between Seyferts and quasars is the amount of radiation from the central source. In optical wavelengths the luminosity typically emitted by a Seyfert central source is similar to that emitted by the sum of the galaxy stars, but in the case of quasars, the luminosity from the source is greater than that of the stars by a factor of at least 100. Hence, in Seyfert galaxies the host galaxy can be seen, but in quasars, host galaxies are difficult to see because of the glare from the quasar. At X-ray wavelengths, the measure usually used is the 2-10 keV luminosity; a quasar has typically $L_{2-10} > 10^{44}$ erg s^{-1} and a Seyfert galaxy has $L_{2-10} < 10^{44}$ erg s^{-1} (e.g. Loaring et al 2003).

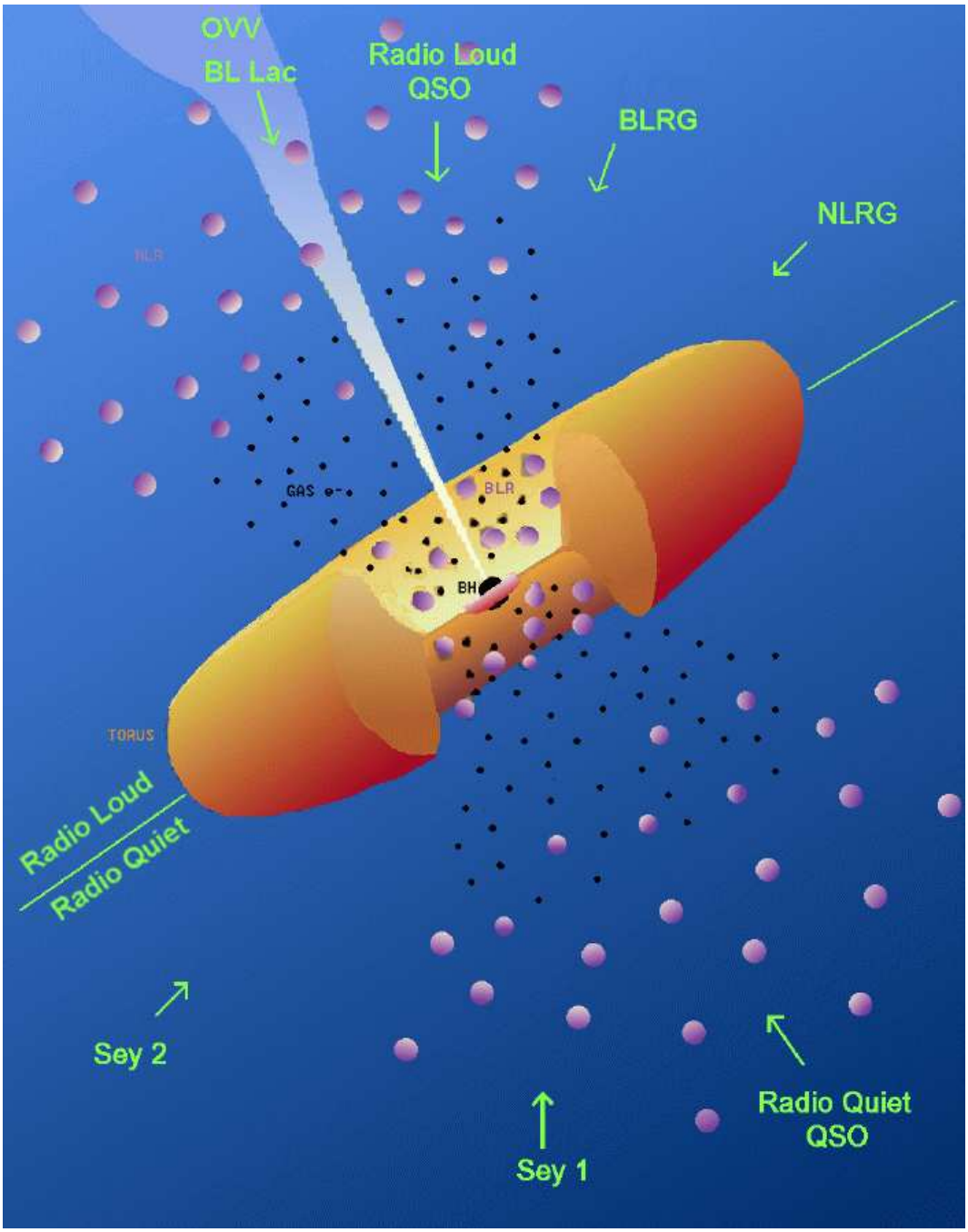

Figure 1.2: The Unified AGN model. Starting at the centre and moving out, we have the black hole, and the accretion disk, viewed through a cut-away part of the obscuring torus. A line of sight not obscured by the torus, so both the BLR (shown as small dark circles) and NLR (shown as large pale circles) are visible, implies a Seyfert 1. A line of sight through the side of the torus, so that just the NLR is visible, implies a Seyfert 2. The accretion disk is of scales of light days, the BLR is of scales of hundreds of light days, the torus is hundreds of light years across, and the NLR is of scales of hundreds of parsecs. The 'top side' of the AGN in this figure is radio-loud, shown by the radio jet, and the 'bottom side' is radio-quiet, as no radio jet is present. For the radio-loud object, the orientations that give rise to narrow line and broad line radio galaxies, radio-loud quasars, and blazars (e.g. OVV and BL Lac objects), viewed directly down the radio jet, are indicated. Radio jets can extend to Mpc scales. Credit for figure: http://isdc.unige.ch/Outreach/Help/help.html

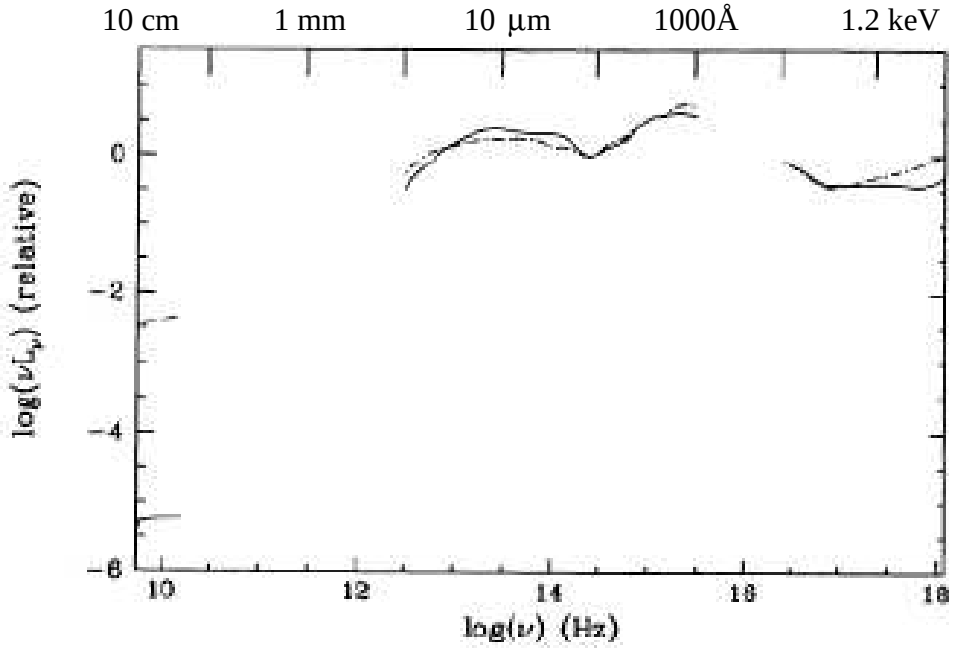

Figure 1.3: Mean spectral energy distributions, normalised at 1.25μm, for radio-loud (dashed line) and radio-quiet (solid line) quasars. Figure from Elvis et al (1994).

1.4 AGN Spectra

1.4.1 Broad-band Spectra

AGN spectra span from the far infrared to hard X-rays, with almost equal power per decade of frequency; radio-loud objects also emit significantly in the radio part. Some of the processes which give rise to the different parts are thermal, i.e. radiation from particles with a Maxwellian velocity distribution. The rest are non-thermal, i.e. radiation from particles whose velocities are not described by a Maxwell-Boltzmann distribution; an example of this is particles that create synchrotron powerlaw spectra, as the distribution of kinetic energy of these particles must also be a powerlaw.

A mean spectral energy distribution for quasars is shown in Fig. 1.3. The radio-loud AGN are seen to lie above the radio-quiet AGN at the hardest X-rays and in the radio.

At energies below 1 keV, there are 2 gaps in the spectra where data are not available; one of these is in the extreme ultraviolet (EUV) part of the spectrum ($\sim 10^{16}$ Hz) and the other is in the millimetre-wavelength regime.

The gap in the EUV is due mainly to the opacity of the ISM in our own Galaxy. The gap at longer wavelengths, the 'millimetre gap', occurs for a few reasons. Between $\sim$ 1 and 300 μm, water vapour absorption in the Earth's atmosphere makes it opaque to infrared and longer wavelengths; however up to $\sim$ 20 μm there are some transparent atmospheric windows. For wavelengths longer than $\sim$ 300 μm, the opacity of the Earth's atmosphere is such that ground-based observations can be done from some very high mountain sites; however, there is a shortage of data due to a lack of sensitive detectors.

The UV/Optical Band

The main feature of the UV/optical spectra of AGN is the 'big blue bump', (e.g. Shang et al 2005), believed to arise from thermal emission in the range $10^{5\pm1}$ K. It covers the wavelength range from $\sim$ 4000 Å to at least 1000 Å. It is not known how strong the big blue bump is in the EUV, as our galaxy becomes almost opaque at wavelengths between 912 Å and $\sim$ 100 Å due to absorption by neutral hydrogen.

The big blue bump is generally thought to be thermal emission from an optically thick, geometrically thin accretion disk. As the disk has a decreasing temperature gradient, moving radially out from the centre, the resulting emission spectrum is roughly a multi-blackbody spectrum.

The Infrared Band

AGN infrared continua are described by a broad, smooth bump between the wavelengths of $\sim$ 2 - 100 μm. The emission can be thermal or non-thermal in origin. A great deal, if not all, of the infrared continuum is thermal emission from dust, illuminated by the AGN. The emission is generally comparable in strength to the

optical - UV, and is far too broad to be explained by a single-temperature grey-body; a range of dust temperatures $\sim$ 50 - 500 K are required. A local minimum at $\sim$ 1 μm implies a thermal emission mechanism in the near infrared. At these wavelengths, thermal emission would require temperatures of $\sim$ 2000 K; this is believed to be emission from the dust closest to the nuclear source ($\sim$ 0.1 pc) e.g. Barvainis (1987).

1.4.2 X-ray Spectra

A main characteristic of AGN is that they emit across the whole electromagnetic spectrum; multiwavelength observations, e.g. Brocksopp et al (2005), are important for constructing a picture of how AGN work as a whole. The X-ray band is extremely important as it allows us to investigate the regions closest to the black hole.

AGN are powered by accretion, but the accretion disk is too cool to produce the observed X-rays. To explain this, a 'corona' (Haardt & Maraschi 1991), is invoked, that consists of a tenuous gas of hot electrons. It is postulated to lie close to the accretion disk. UV photons from the accretion disk are upscattered several times by the electrons in the corona and boosted in energy through the inverse Compton effect. The hot electrons in the corona have a powerlaw distribution of energy; this gives rise to the power law shape of the continuum, in which the number of photons per unit energy E is proportional to $E^{-\Gamma}$, Γ being the photon index.

Sometimes we see a reflection component, which peaks between about 20 and 50 keV. The shape of this reflection 'hump' is due to two mechanisms. One is Compton down-scattering of energetic photons, which recoil off lower-energy electrons in comparatively cold material, such as the outer parts of the accretion disk or the torus. In doing so they lose energy, resulting in a spectral fall-off at high energies (E $>$ 50 keV). At lower-energies ($<$ 10 keV), the photoelectric absorption

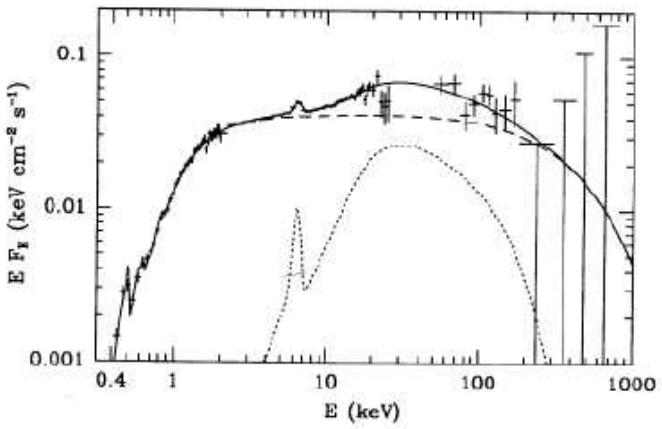

Figure 1.4: A broad-band spectrum of IC 4329A, denoted as crosses. The dashed curve gives the incident spectrum, the dotted curve shows the reflection component including a fluorescent Fe Kα line, and the solid line denotes the sum. Figure from Magdziarz & Zdziarski (1995).

cross-section is much larger than the cross-section for Compton scattering in cool material, so photoelectric absorption prevents reflection. These aspects combine to create the hump-like feature.

A spectrum of the Seyfert 1.2 IC 4329A is shown in Fig. 1.4. Also shown in this Figure are the best-fit model components that demonstrate how the shape of the spectrum arises. The absorbed incident spectra is distorted by the underlying reflection.

Often an iron Kα line at 6.4 keV, formed by fluorescence, is present; one is clearly present in Fig. 1.4. Fluorescence is a process whereby an atom's inner-shell electron is knocked out by a high-energy photon; following this, two things can happen. An M-shell electron can drop down and fill the vacancy, with the emission of a photon; or, as the ion is in an excited state, an outer shell electron can be emitted. The latter event is known as the Auger effect, and the ejected electron is known as an Auger electron. The probability that a photon is emitted rather than an Auger electron is known as the fluoresence yield; iron has the highest fluoresence yield, of 34 %. Iron Kα lines are often present in AGN and in particular are present in all objects studied in this thesis. A review of reflection

and AGN iron lines is given in Fabian et al (2000).

In most sources an excess of emission above the extrapolated power law, below ~ 1 keV in the soft X-ray band, is seen; this is known as the 'soft excess'. One theory for this component is that it is an extension of the big blue bump, seen in the UV, that comes from the accretion disk.

1.5 Absorption

1.5.1 Cold absorption

Cold absorption from our own Galaxy is always present in X-ray spectra, but sometimes there is additional cold absorption. This could originate in a variety of locations, e.g. the host galaxy of the AGN or cold material near the AGN. Such additional cold absorption occurs in the spectra of H 0557−385 and is discussed in Chapter 3, but does not occur in PG 1114+445 or PG 1309+355.

1.5.2 Warm absorption

Warm absorbers are clouds of ionised gas intrinsic to AGN. They were first suggested by Halpern (1984) to explain *Einstein* data of the quasar MR 2251-178. They are dubbed 'warm' absorbers as they imply gas at temperatures of $\sim 10^4 - 10^5$ K (Krolik & Kriss 2001); the gas is photoionised, not collisionally ionised. High resolution observations of warm absorbers have shown that they are outflowing (e.g. Kaastra et al 2000, Reeves et al 2003). The abundances of different elements can also be derived from spectroscopy (e.g. Blustin et al 2002).

The spectral sign of a warm absorber is a deficit of counts in the soft X-ray part of the spectrum with respect to the extrapolation of a power law fit carried out at energies above ~ 2 keV.

Warm absorbers were found to be of importance in the study of AGN following a study of 24 type 1 AGN (Reynolds 1997), which showed them to be present

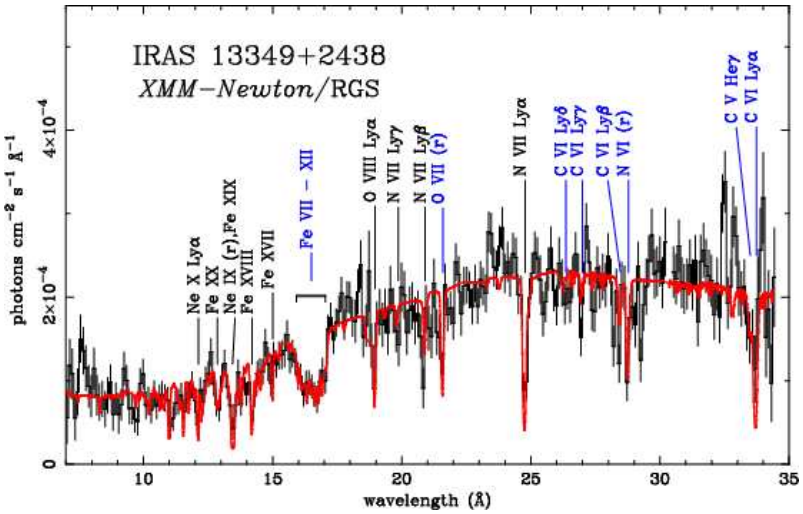

Figure 1.5: The RGS spectrum of IRAS 13349+2438, in the rest-frame. The iron UTA is obvious. Features labelled in blue are mainly produced in the low-ionisation component, features labelled in black are from the high-ionisation component. Figure from Sako et al (2001).

in half of the sample. Data from the CCD cameras on *ASCA* led astronomers to believe that the spectral signature of warm absorbers was in the form of deep OVII and OVIII edges (e.g. George et al 1997). Only the advent of *XMM-Newton* and *Chandra* with their high resolution spectrometers revealed that in fact warm absorbers imprint a series of narrow absorption lines on spectra; this was seen for the first time in the *Chandra* spectrum of NGC 5548 (Kaastra et al 2000). Many warm absorbers have since been observed at high resolution, e.g. IRAS 13349+2438 (Sako et al 2000); NGC 3783, NGC 7469 (Blustin et al 2002, 2003); IC 4329A (Steenbrugge et al 2005).

High-resolution observations of warm absorbers with XMM-Newton and Chandra found that at soft X-ray energies, inner-shell absorption by M-shell iron ions in the form of unresolved transition arrays (UTAs) is seen in some AGN spectra; the first UTA to be identified was in the quasar IRAS 13349+2438 (Sako et al 2001; see Fig. 1.5). The presence of a UTA denotes a 'cold' phase of a warm absorber, and the location of a UTA in a spectrum can be used to determine the ionisation state of the gas (Behar et al 2001).

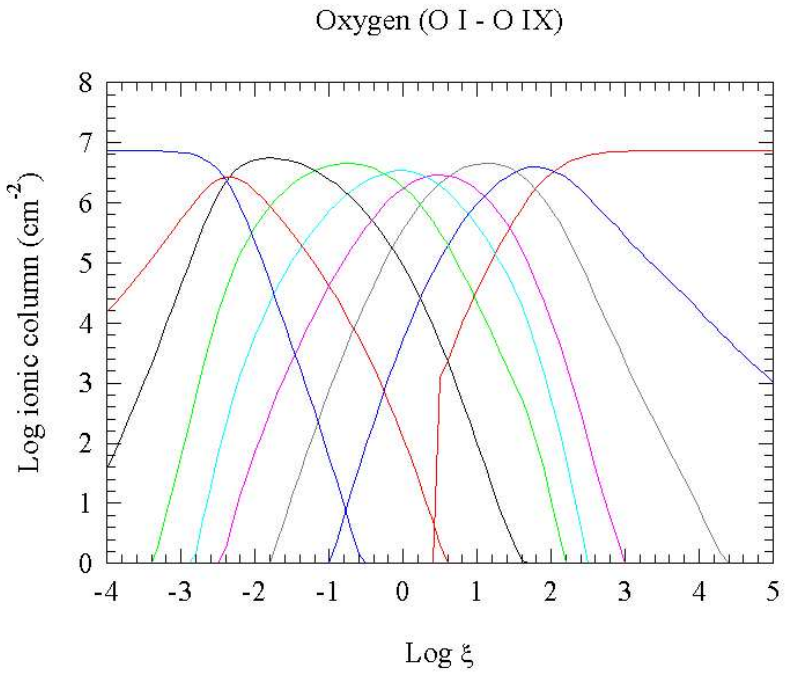

Figure 1.6: The ionic abundance for oxygen, versus ξ, within a photoionised plasma. The curves from left to right correspond to increasingly ionised oxygen, from O I - O IX. Credit for figure: Jelle Kaastra, SRON.

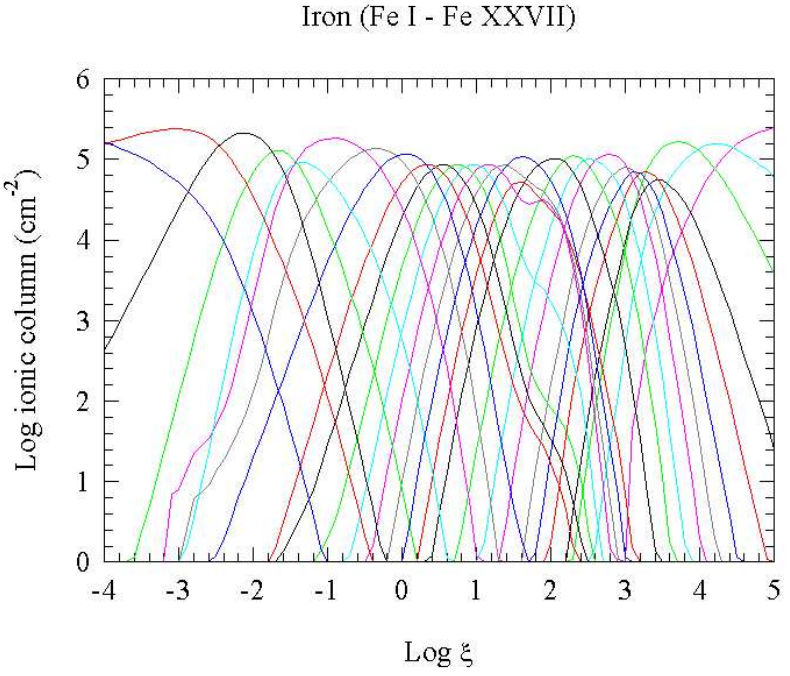

Figure 1.7: The ionic abundance for iron, versus ξ, within a photoionised plasma. The curves from left to right correspond to increasingly ionised iron, from Fe I - Fe XXVII. Credit for figure: Jelle Kaastra, SRON.

In most observations, it is found that more than one 'phase' of warm absorber is present. Two phases were proposed for IRAS 13349+2438 (Sako et al 2000), whereas Steenbrugge et al (2003) find three phases of warm absorber in NGC 5548. We define a phase as gas at a particular ionisation parameter, ξ, and column density. We define the ionisation parameter as $\xi = L/nr^2$ in erg cm s^{-1} (Tarter et al 1969). Here L is the ionising luminosity (erg s^{-1}, taken to be the 1-1000 Rydberg luminosity), n the gas density (cm^{-3}), and r the distance of the ionising source from the absorbing gas, in cm.

Fig. 1.6 and Fig. 1.7 show the ionic abundances of oxygen and iron, respectively, for a photoionised plasma. Both ions are important in AGN absorption spectra, oxygen being highly abundant and contributing much absorption, and iron forming a UTA if the ionisation parameter is in the right range. OVII is most abundant at log ξ values of 1, whereas OVIII is most abundant nearer log ξ values of 2. The ionisation parameters that lead to an M-shell UTA of iron (Fe X - Fe XVI) are $\sim$ 0-2.

1.5.3 The origins of warm absorbers

There are currently two main theories for the origins of warm absorbers. One explanation is a wind formed by photoionised evaporation from the inner edge of the torus (Krolik & Kriss 2001), lying a few parsecs from the continuum source. Reynolds (1997) suggests that 'outer' absorbers may be a radiatively driven dusty wind from the torus; it could be ionised material on the inner edge of the torus, driven by radiation pressure which would give it a conical shell-like structure.

Another possibility is a wind driven off the accretion disk. By analogy with winds from hot stars, Castor, Abbott & Klein (1975) consider the force exerted on stellar material as result of absorption and scattering of line radiation, thought to be responsible for the outflow of material in massive hot stars. From the concept that momentum is extracted most efficiently from the radiation field via

line opacity, Castor, Abbott & Klein (1975) show that a great number of lines from many different elements contribute to the total force. Applying the concept of such a wind to AGN, Proga et al (2000) find that a disk accreting around a 10^8 $M_\odot$ black hole can launch a wind at $\sim 10^{16}$ cm from the central engine. Elvis (2000) finds that an accretion disk wind, viewed at different angles, will explain the many varieties of absorption features seen in quasars.

As for the geometry of warm absorbers, recent high-resolution X-ray observations of the Seyfert 2 NGC 1068 (Kinkhabwala et al 2002; Brinkman et al 2002) suggest that in this source we are viewing the warm absorber in emission, in the shape of an ionisation cone. Kinkhabwala et al (2002) find that the column densities and ionisation parameters observed in Seyfert 2s are consistent with those found in warm absorbers in Seyfert 1 AGN. Fig. 1.8 shows a cartoon of the ionisation cone of NGC 1068.

1.5.4 Warm absorbers in Quasars and Seyfert AGN

Warm absorbers are common in Seyferts: in the study mentioned above of 24 type 1 AGN, of which 18 are Seyfert galaxies, half were found to have warm absorbers (Reynolds 1997). However, they are far rarer in quasars. In a study of 23 quasars, only one was found to display warm absorption (Laor 1997). So, is there any physical difference in the warm absorbers observed in different types of AGN?

Relativistic outflows have been reported for the quasars PG 0844+349 (Pounds et al 2003a), PG 1211+143 (Pounds et al 2003b) and PDS 456 (Reeves et al 2003). These authors find that the absorber can, in each case, be modelled with a single, very high ionisation parameter, much higher than is usually found in quasars or Seyferts; however, Kaspi et al (2004), using the same data, suggest that the absorption lines in PG 1211+143 imply an outflow of just 3000 km s^{-1}, instead of 24,000 - 30,000 km s^{-1} as suggested by Pounds et al (2003b). But such fast

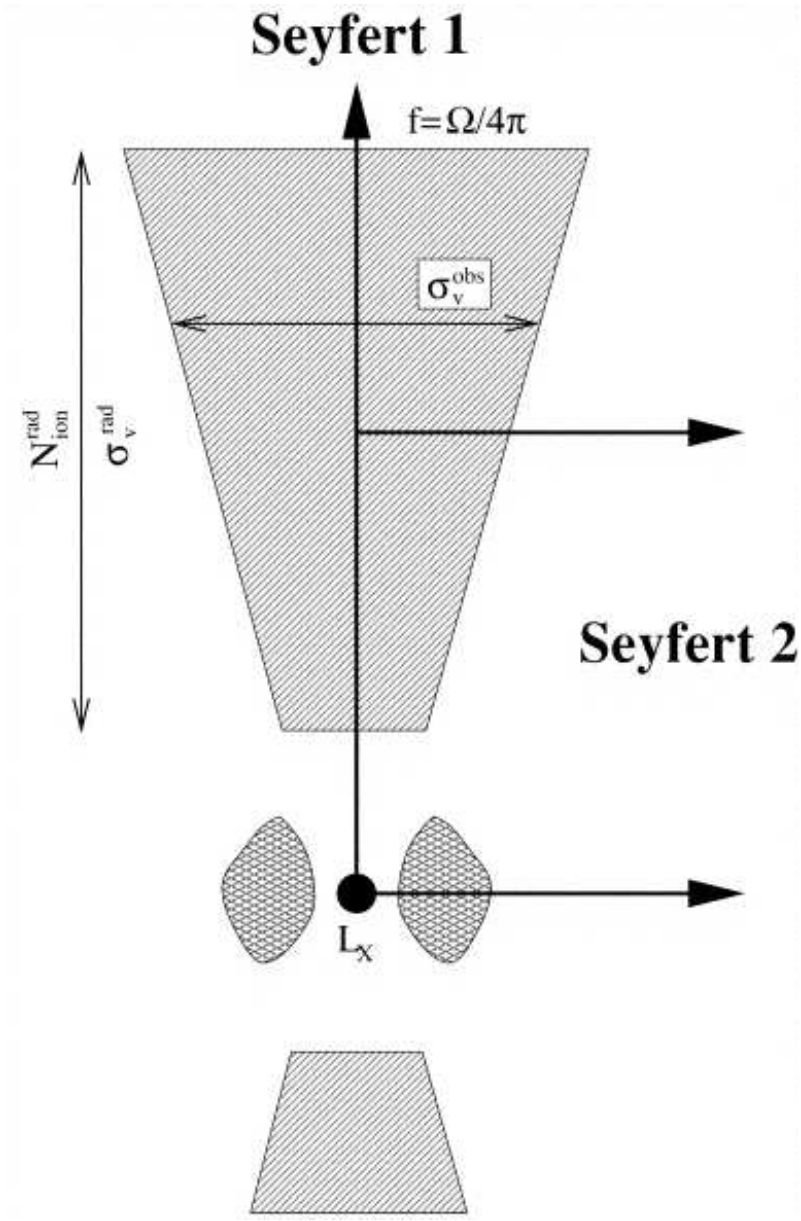

Figure 1.8: A cartoon of the ionisation cone of NGC 1068 (not to scale). The black dot represents the central source. For a Seyfert 1, the ionisation cone comprising the warm absorber is observed end-on as it absorbs the central source radiation. For a Seyfert 2, the torus (shown as blobs either side of the central source, cut away to show the source) absorbs the radiation from the central source, and the ionisation cone is seen in emission. Figure from Kinkhabwala et al (2002).

outflows are by no means found in all quasar warm absorbers, so they are not necessarily representative.

From a detailed study of the warm absorbers in 23 AGN, Blustin et al (2005) find that bolometric luminosity is not correlated with average ionisation parameter; neither is it correlated with total column. If PG 0844+349 and PG 1211+143 are ignored, then the average outflow speeds are not greatly correlated with bolometric luminosity, column or average ionisation parameter. There seems to be no defining difference between the warm absorbers seen in different types of AGN.

1.5.5 Where are warm absorbers located in AGN?

Locating the positions of warm absorbers in AGN has been found to be tricky. At present, no definitive idea exists of where warm absorbers live in the structure of AGN; Krolik & Kriss (2001) speculate that they could lie anywhere from the broad-line region, to tens of parsecs out. Hence their origins are essentially unconstrained, which is one of the motivations for the research in this thesis.

If a warm absorber is a wind from the inner edge of the torus (Krolik & Kriss 2001), then it will exist a few parsecs from the continuum source; on the other hand, if it is a wind driven off the accretion disk, Proga et al (2000) find that it can be launched at $\sim 10^{16}$ cm from the central engine.

The ionisation cone scenario suggested for the Seyfert 2 NGC 1068 (Kinkhabwala et al 2002; Brinkman et al 2002), which means we see the warm absorber in emission in this type of galaxy, places it at the distance of the NLR of the AGN, at hundreds of pc.

From their sample of 23 AGN, Blustin et al (2005) find that warm absorbers are most likely to originate as outflows from the torus. For the absorber of PG 1114+445, Mathur et al (1998) find the absorber eats into emission lines, placing it outside the BLR; they put an upper limit of 4×10^{17} cm for the distance of the absorber. However, from the 900ks *Chandra* observation of NGC 3783,

Netzer et al (2003) obtain lower limits of 3.2, 0.6 and 0.2 pc for the distances of the three separate absorbers found.

1.5.6 UV and X-ray warm absorbers

It has been hypothesised for some time now that there are strong relations between X-ray and UV absorbers, or maybe even that they both have a common origin. The evidence for this has been gathering ground recently.

Observationally, Mathur, Wilkes & Elvis (1998) model the absorption in PG 1114+445 with a single UV and X-ray absorber. They found that the outflowing velocity of both the X-ray and UV absorbers is 530 km s^{-1}, and that the derived ion column densities from both absorbers agree.

Convincing evidence comes from the study by Crenshaw et al (1999), who found that there is a 1:1 correlation of UV absorbers and X-ray absorbers. Their study found that in most cases the UV absorbers are outflowing, as are the X-ray absorbers; the cores of the strong absorption components are much deeper than the continuum flux levels, which indicates that the absorption components exist completely outside of the broad emission-line regions. From the sample it is induced that the intrinsic absorbers cover a large part of the sky ($\geq 50\%$) as seen from the continuum source.

What processes take place for a wind to arise? Close in to the central source, the gas is over-ionised and few atomic transitions are available, so electron scattering prevails. This cannot drive a wind alone, and this 'failed' wind then acts to screen the gas further out from the central source. In doing so, the ionisation parameter is lowered; when it falls below a certain value, the number of transitions and the opacity rises very fast, making the radiation and line driving $\sim$ 1000 times stronger than just electron scattering, and a wind is formed. Most of the UV and soft X-ray continuum is absorbed by the wind (Elvis 2004).

From hydrodynamical calculations of line-driven winds from AGN, Proga et al

(2000) find that local disk radiation can launch a disk wind, even in the presence of strong ionising radiation from the central object. This central radiation may cause the part of the flow to be over-ionised, and slow the wind down. The X-ray opacity of the wind must be much higher than the UV opacity, in order to create a fast wind. So that the stream is optically thin to the UV radiation but optically thick to X-rays, a typical column density radially through the fast stream is a few 10^{23} cm^{-2}. For a disk accreting around a 10^8 M$_\odot$ black hole, a wind can be launched at $\sim 10^{16}$ cm from the central engine; then for a reasonable X-ray opacity, the wind can be accelerated by the central UV radiation to velocities of up to 15000 km s^{-1}.

1.6 The XMM-Newton observatory

The *XMM-Newton* spacecraft (Jansen et al 2001) is the largest scientific satellite ever launched by the European Space Agency. With a total effective area of $\sim$ 4500 cm^2 (1500 cm^2 at 1 keV per telescope, x 3 telescopes), it has much greater sensitivity than *Chandra* (collecting area of 800 cm^2 at 0.25 keV and 400 cm^2 at 5 keV); in fact *XMM-Newton* has more than ten times the effective area than *Chandra* at $\sim$ 6-7 keV, a very important energy band for the study of the K-shell transitions of iron. In contrast, *Chandra* has higher spatial resolution, with 0.5″ FWHM from the HRC (High Resolution Camera), compared to a spatial resolution of 6″ FWHM from the EPIC instruments on *XMM-Newton*.

Each of *XMM-Newton's* three X-ray telescopes is made of 58 closely packed mirror shells to get the highest effective area. Operating in a 48 hour eccentric orbit, *XMM-Newton* provides uninterrupted observing capability for up to 40 hrs. The spacecraft houses three imaging X-ray instruments. At the primary focus of the 3 telescopes, there are 3 EPIC (European Photon Imaging Camera) CCD cameras. Two are EPIC MOS cameras (Turner et al 2001), employing arrays of Metal-Oxide-Silicon (MOS) X-ray sensitive CCDs; one is an EPIC pn

camera (Strüder et al 2001), with a pn CCD. They provide imaging and medium resolution spectroscopy. Associated with the two telescopes with MOS cameras are the high-resolution RGSs (Reflection Grating Spectrometers; den Herder et al 2001). Both RGS chains incorporate an array of gold-coated reflection gratings that deflect about half the light incident on them, whilst allowing the other half to be transmitted to the primary focus where the MOS cameras are located. The EPIC pn telescope has no gratings behind it, so the pn camera receives all the X-ray flux. Co-aligned with the X-ray instruments is the optical monitor (Mason et al 2001), a 30cm optical/ultraviolet telescope.

The spatial resolution of EPIC is such that the in-orbit measured Point Spread Function half-energy width, within which half of the light from the telescopes is focussed, is 15.2″ for pn, 13.8″ for MOS1 and 13.0″ for MOS2. Later in this thesis I extract spectra by selecting source photons within circles of radius 25-30″. For the EPIC instruments, 30″ corresponds to $\sim$ 80% fraction encircled energy.

The EPIC cameras take imaging spectroscopy over the telescope's field of view (FOV) of 30 arcmin and in the energy range 0.15 to 15 keV, with moderate spectral resolution ($E/\Delta E \sim$ 20-50). All the CCDs of the EPIC instruments produce data in the form of event lists, that is, tables with one entry line per received event, listing the positions at which the photons were registered, their arrival times and their energies.

The MOS detectors are most efficient in the 1-5 keV range. As they only have a 40-micron sensitive depth of silicon, the detectors are less responsive to hard X-rays. Each MOS CCD consists of seven silicon chips, each made up of a matrix of 600 x 600 pixels (1 pixel = 1.1″).

The PN camera, with a 300-micron thickness of silicon, registers hard X-rays better than the MOS camera. Also in contrast to the MOS camera, the PN detector has a 400 x 400 pixel matrix of size 6 cm x 6 cm (1 pixel = 4.1″).

One important practical difference between the MOS and pn cameras is their time resolution. The pn has a much higher time resolution, as each pixel column

in the pn camera has its own readout node. In full-frame mode, the MOS reads out in 2.6s, whereas for the pn, the parallel readout of channels enables the camera to be operated quickly: in full-frame mode, only 73 ms are needed to acquire one frame.

The type of illumination of the chips also affects the quantum efficiency (QE), defined as the fraction of incident photons on the detector that generate an event in the CCD. The QE differs between the MOS and pn CCDs: the QE of the pn CCDs is higher than that of the MOS CCDs, see Fig. 1.9 and Fig. 1.10. As the pn CCD is illuminated from the rear side (back-illuminated), which does not have insensitive layers or coatings, the X-ray detection efficiency is extremely high and homogeneous from the very low to the highest energies (over 90% from 0.5 to 10 keV).

The RGS is designed for high spectral resolution measurements in the soft X-ray range, where the K-shell transitions of C, N, O, Ne Mg, Si, S and C, and also the L-shell transitions of Fe are located. It allows detailed line diagnostics, and from such measurements the density, temperature, ionisation state and chemical composition of the sources observed can be determined. RGS has much higher energy resolution ($E/\Delta E \sim$ 200-800 over an energy range 0.3-2.1 keV) than EPIC ($E/\Delta E \sim$ 20-50, energy range of 0.1-15 keV).

The RGS spectrum is dispersed in wavelength so individual lines and line profiles can be resolved. The reflection gratings are basically mirrors with many tiny grooves on them. The gratings are covered with a gold layer and there are 600 grooves per millimeter. The light from the telescope grazes off the plates, and diffraction occurs in the beams reflected from the grooves. For a given spectral order, the angle of reflectance is greater for longer wavelengths, producing a dispersed spectrum.

The X-rays dispersed into a spectrum are focussed on the two RGS cameras. The position of an X-ray of wavelength λ on the CCD array is given by the dispersion equation

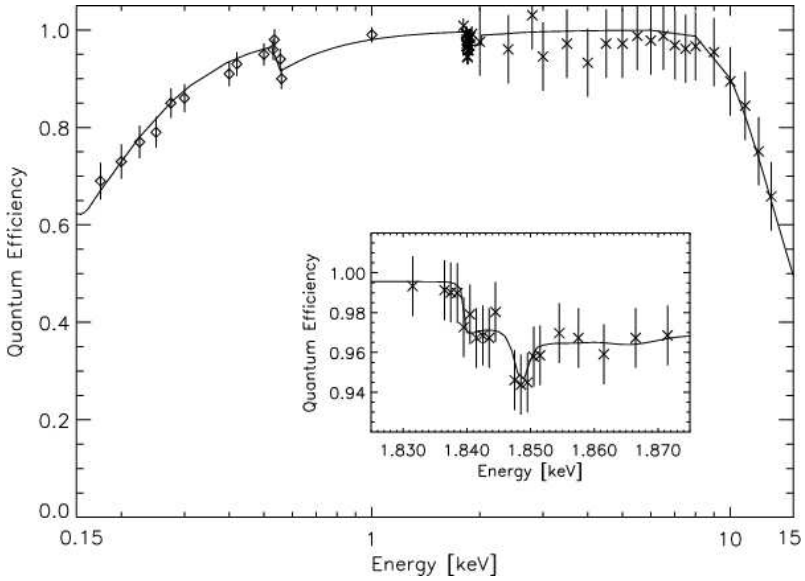

Figure 1.9: Quantum Efficiency of the pn CCD (Strüder et al 2001)

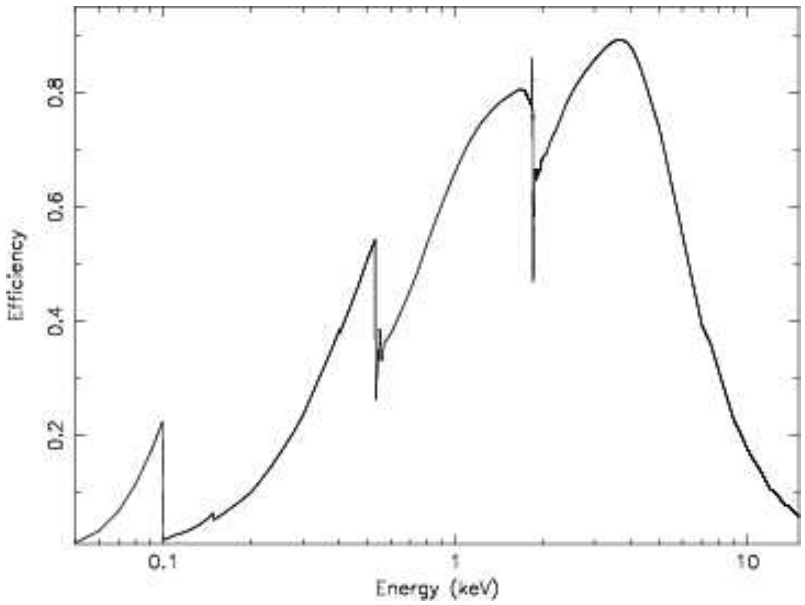

Figure 1.10: Quantum Efficiency of the MOS CCD (Turner et al 2001)

$n\lambda = d(\cos\beta - \cos\alpha)$

Here, n is the spectral order with values -1, -2 etc, d is the groove spacing, and α and β are the angles made by incident and dispersed rays with the grating plane respectively. Because of the RGS particular optical design, the spectral orders overlap, but the CCDs have sufficient energy resolution to separate photons in different orders.

1.6.1 Pile-up

Pile-up happens when a bright source is being observed and there is the possibility that two or more X-ray photons hit the same CCD pixel or adjacent pixels during one read-out cycle. If this happens, the events are read out as one single event with the sum of the energies. The different event possibilities are thus labelled in the EPIC data analysis:

Single event: charge spread over 1 pixel (pattern = 0)
Double event: charge spread over 2 pixels (pattern = 1-4)
Triple event: charge spread over 3 pixels (pattern 5-6)
Quadruple event: charge spread over 4 pixels (patterns 9-12)

For all the sources considered in this thesis, the pn spectra were accumulated using single and double events, corresponding to PATTERN values of 0-4, and the MOS spectra were constructed using all valid events (PATTERN = 0-12).

1.6.2 Filters and window modes

EPIC has thick, medium and thin filters for blocking optical light; so for each observation a suitable filter is chosen to sufficiently suppress the optical contamination.

EPIC also has different window modes in order to reduce the field-of-view

electronically to reduce the readout rate and hence improve the time resolution: this increases the pile-up count-rate limit for bright sources (Strüder et al 2001).

Chapter 2

PG 1114+445 and PG 1309+355

PG 1114+445 is a radio-quiet quasar that was listed in the Bright Quasar Survey (BQS, Schmidt & Green 1983) and belongs to a subset of 23 quasars in the BQS with z $\leq$ 0.4 and Galactic $N_H \leq 1.9\times10^{20}$ cm^{-2} (Laor 1997). PG 1114+445 has a redshift of 0.144 and Galactic N_H of 1.83×10^{20} cm^{-2} (Dickey & Lockman 1990).

The presence of a warm absorber in PG 1114+445 is well known. Using *ROSAT* and *ASCA* data, George et al (1997) model the absorption in PG 1114+445 as OVII and OVIII edges, and determine the column density of the ionised gas to be $\sim 2\times10^{22}$ cm^{-2}. Mathur et al (1998; hereafter M98) find that the absorber lies outside the BLR, or is cospatial with it, and has a mass outflow rate of 1 $M_\odot$ yr^{-1}.

As found by Reynolds (1997), significant absorption could occur for $\sim$ 50% of lower-luminosity AGNs, wheras it is rare for quasars, occuring for less than 5% of the subset of Laor (1997). Crenshaw et al (1999) find that there is a one-to-one correlation of UV and X-ray absorbers in Seyfert galaxies; both X-ray and UV absorption have been observed in PG 1114+445. The HST spectrum of M98 shows strong UV absorption lines blueshifted by $\sim$ 530 km s^1 from the systemic redshift of the quasar.

PG 1309+355 is a radio-intermediate AGN that was listed in the BQS. A warm absorber has not been detected in this source prior to the *XMM-Newton*

Table 2.1: Galactic column densities and observation details. Obs. Date is Observation Date, Gal. N_H is Galactic N_H in units of $10^{20}cm^{-2}$ and Eff. Exp. Time is Effective Exposure Time.

Quasar	Obs. Date	Redshift	Gal. N_H 10^{20} cm^{-2}	Eff. Exp. Time (ks)	Count Rate (Counts s^{-1})
PG 1114+445	15.05.02	0.144	1.83	PN:37, MOS:42	PN:0.67, MOS:0.20
PG 1309+355	10.06.02	0.184	1.03	PN:23, MOS:29	PN:0.50, MOS:0.13

observation. PG 1309+355 lies at a redshift of 0.184 and has a Galactic N_H of 1.03×10^{20} cm^{-2} (Dickey & Lockman 1990).

2.1 XMM-Newton observations

PG 1114+445 and PG 1309+355 were observed with *XMM-Newton* (Jansen et al 2001) as part of the *OM* Guaranteed Time programme. The EPIC observations of both objects were done using the thin filter, with the cameras in large window mode.

Table 2.1 summarises the Galactic column densities (from Dickey & Lockman 1990), the redshifts (from L97), and observation details. The *RGS* data do not contain enough counts for us to construct a useful spectrum for either quasar.

The *EPIC* data were taken in large window mode, and using the thin filter. The data were processed using the Science Analysis System (SAS) Version 5.4.1; the *pn* spectra were constructed using single and double events, corresponding to pattern values of 0-4, and the *MOS* spectra were constructed using all valid events (PATTERN = 0-12).

The count rates are well below the thresholds (12 counts s^{-1} for the *pn* and

1.8 counts s^{-1} for the *MOS*) where pile-up has to be considered for large window mode. Events next to bad pixels and next to the edges of CCDs were excluded (FLAG = 0 in SAS). The source spectra were constructed by taking counts within a circle of radius 25 arcsec around PG 1114+445 and 30 arcsec around PG 1309+355. In each case, background spectra were extracted from nearby source-free regions with three times the radius of those used to extract the source spectra. Periods of high background, identified in 5-10 keV lightcurves for the whole field of view outside the source circle, were excluded from further analysis.

The quasar spectra were grouped with a minimum of twenty counts per channel, to allow χ^2 statistics to be used. Response matrix files (RMF) and auxiliary response files (ARF) for each instrument were generated using the *SAS*. The *EPIC MOS* and *pn* data were coadded using the method of Page, Davis & Salvi (2003). The data were modelled using *SPEX* 2.00 (Kaastra et al 2002). I adopt a cosmology with $H_0 = 70.0$ km s^{-1} Mpc^{-1}, $\Omega_m = 0.3$ and $\Omega_\lambda = 0.7$.

2.2 Initial fitting

To begin, both quasar spectra were fitted over the 0.3-10.0 keV energy range with a simple model, consisting of a power law and Galactic absorption. The parameters for these fits are shown in Table 2.2.

Figs 2.1 - 2.8 show the spectra and data/model ratios for the combined *pn* and *MOS* data of each quasar. All spectra are plotted in the observed frame, unless otherwise stated. During the spectral fitting, neutral Galactic absorption was held fixed at the values shown in Table 2.1.

As seen in Fig. 2.1, a power law was a poor fit to the *EPIC* data of PG 1114+445, with a highly unacceptable χ^2/dof of 5.38 for 832 dof. Similarly, a power law fit to *EPIC* data of PG 1309+355 yields an unacceptable χ^2/dof of 1.63 for 456 dof, shown in Fig. 2.5. A warm absorber is indicated because at $\sim$ 0.6 - 1 keV in

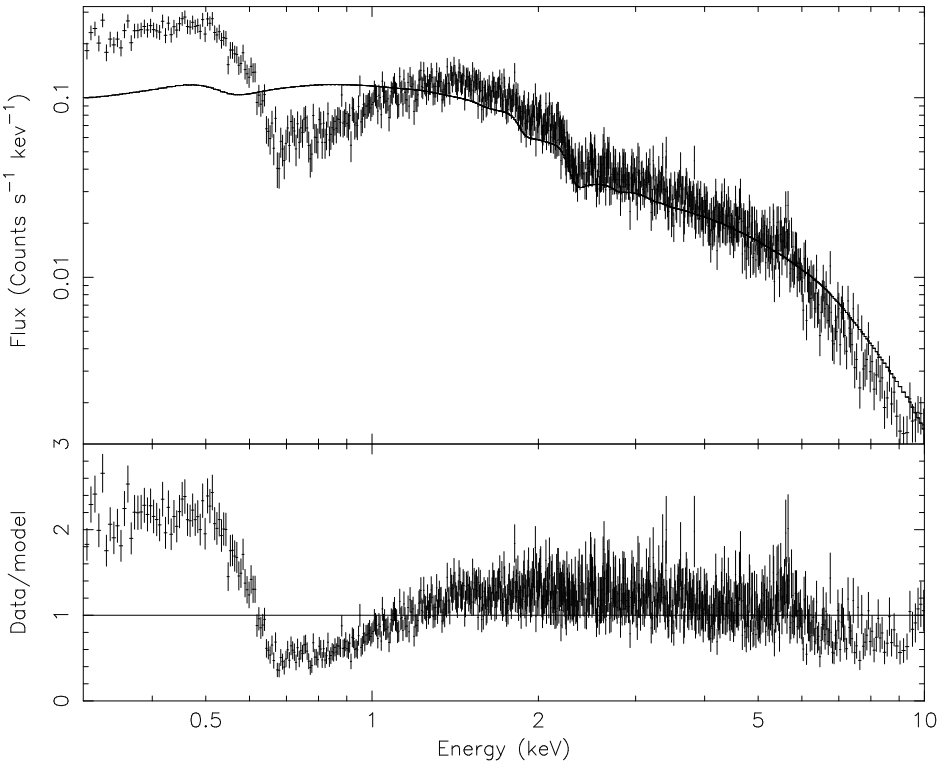

Figure 2.1: PG 1114+445: Power law fit.

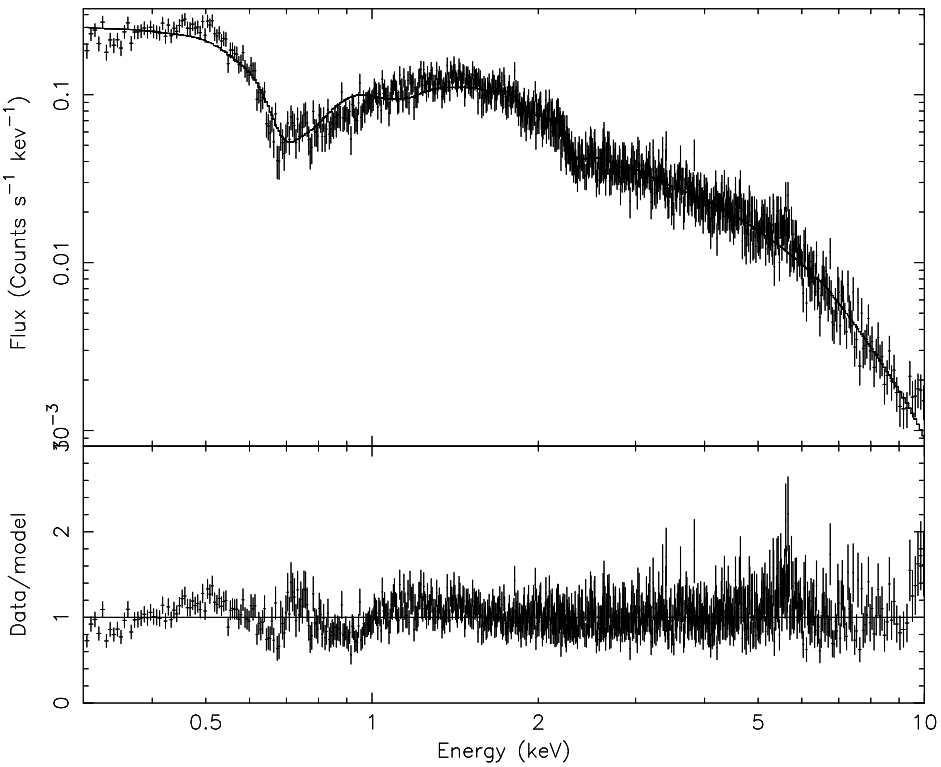

Figure 2.2: PG 1114+445: Fit with single warm absorber.

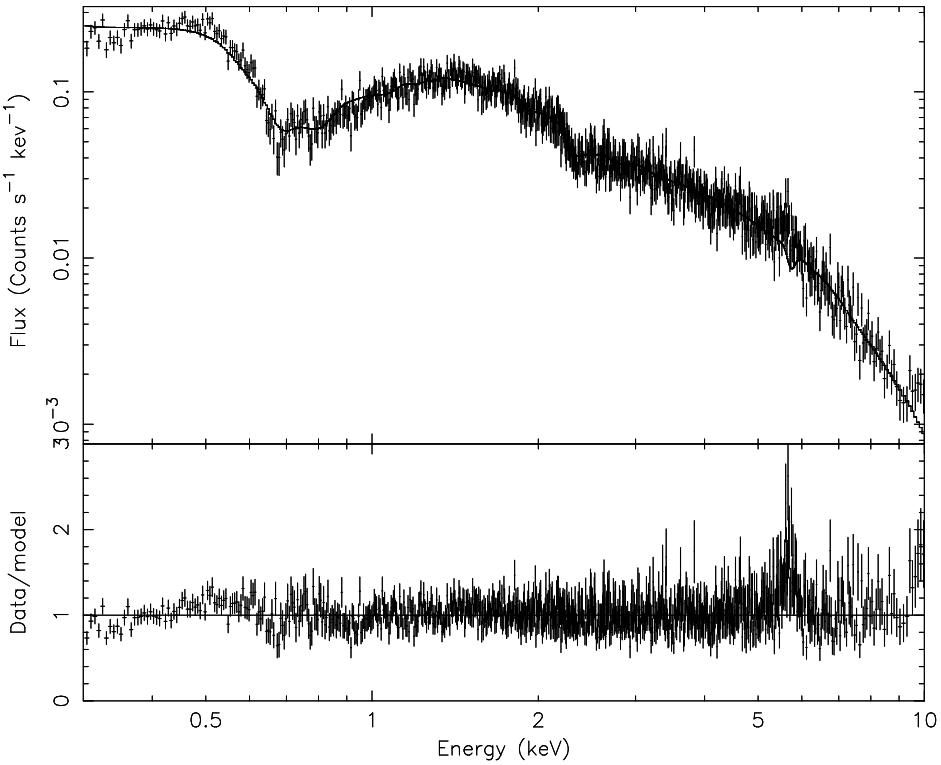

Figure 2.3: PG 1114+445: Fit with two warm absorbers.

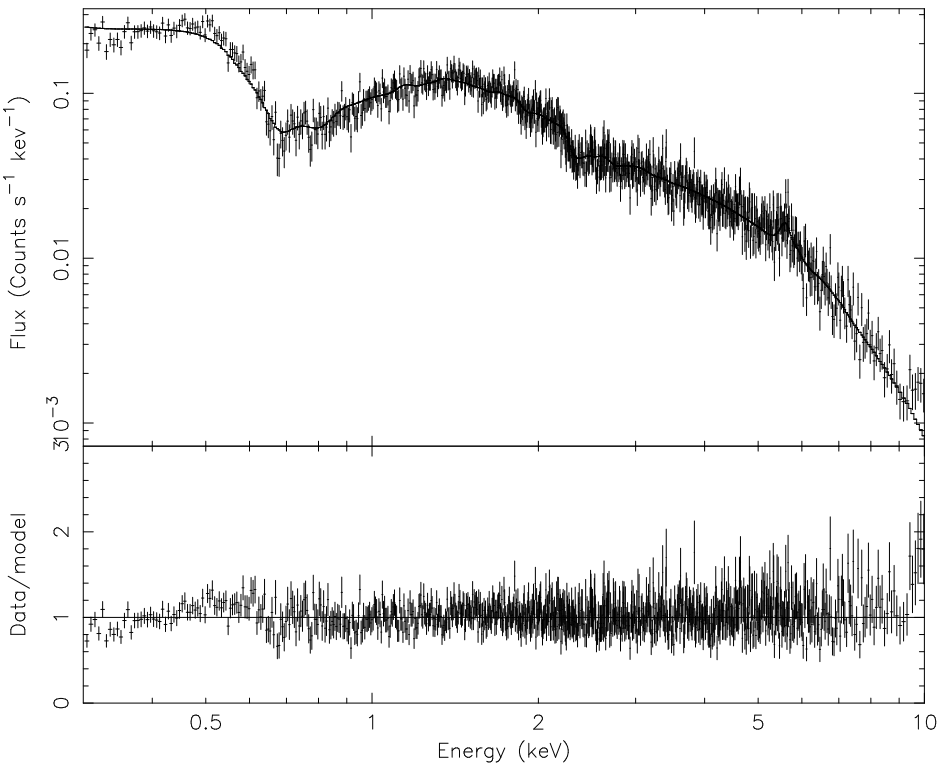

Figure 2.4: PG 1114+445: Fit with two warm absorbers and iron Kα line.

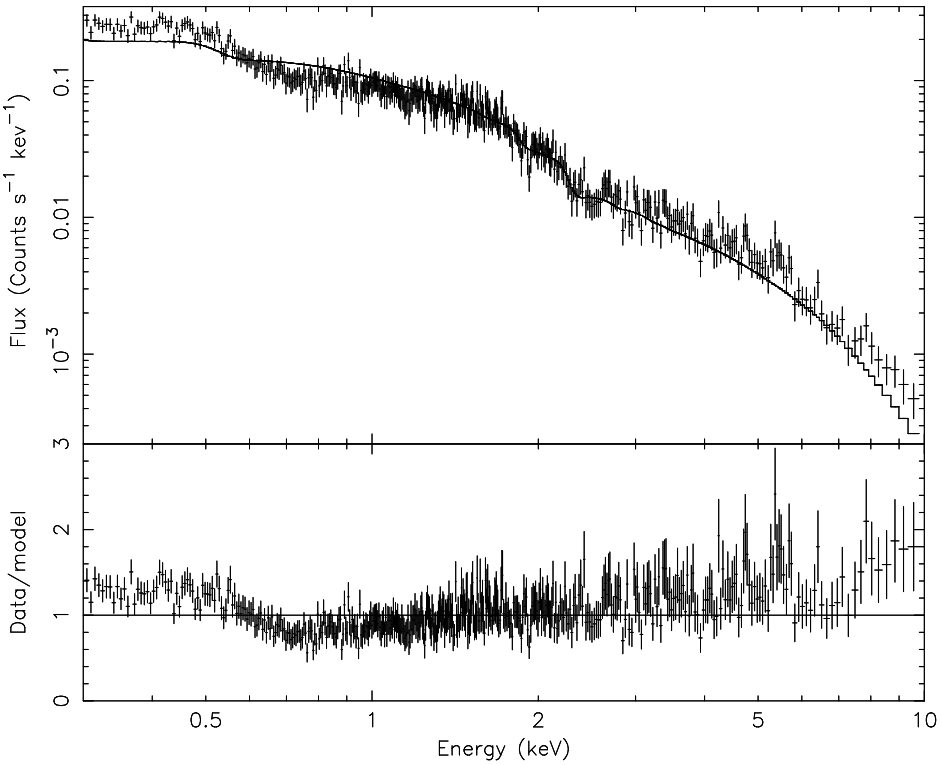

Figure 2.5: PG 1309+355: Power law fit.

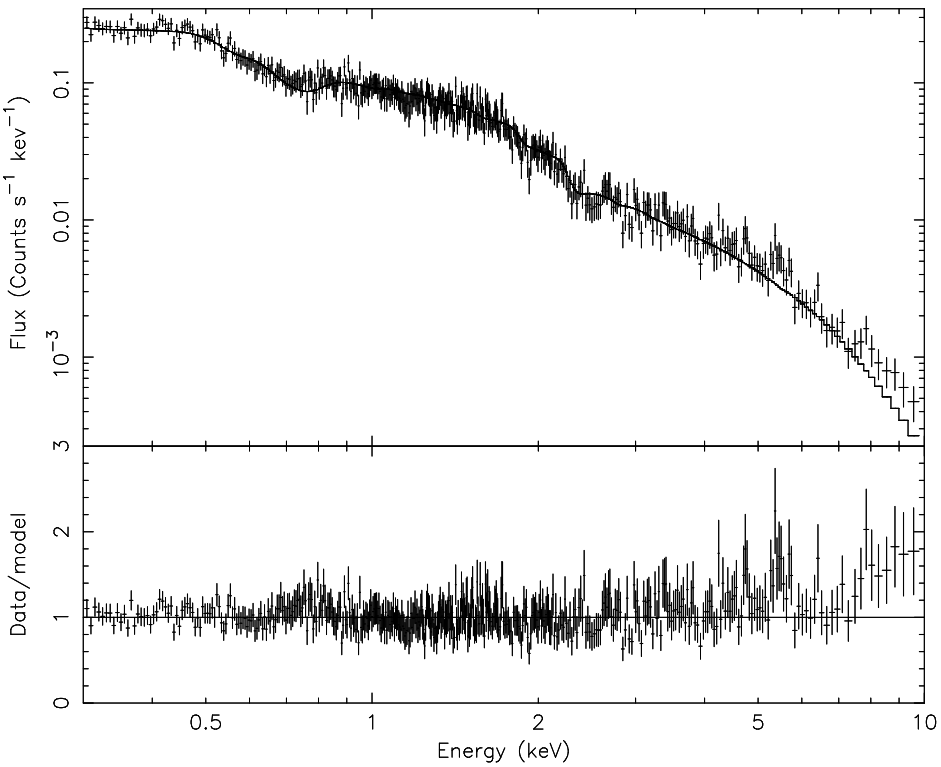

Figure 2.6: PG 1309+355: Single warm absorber fit without blackbody.

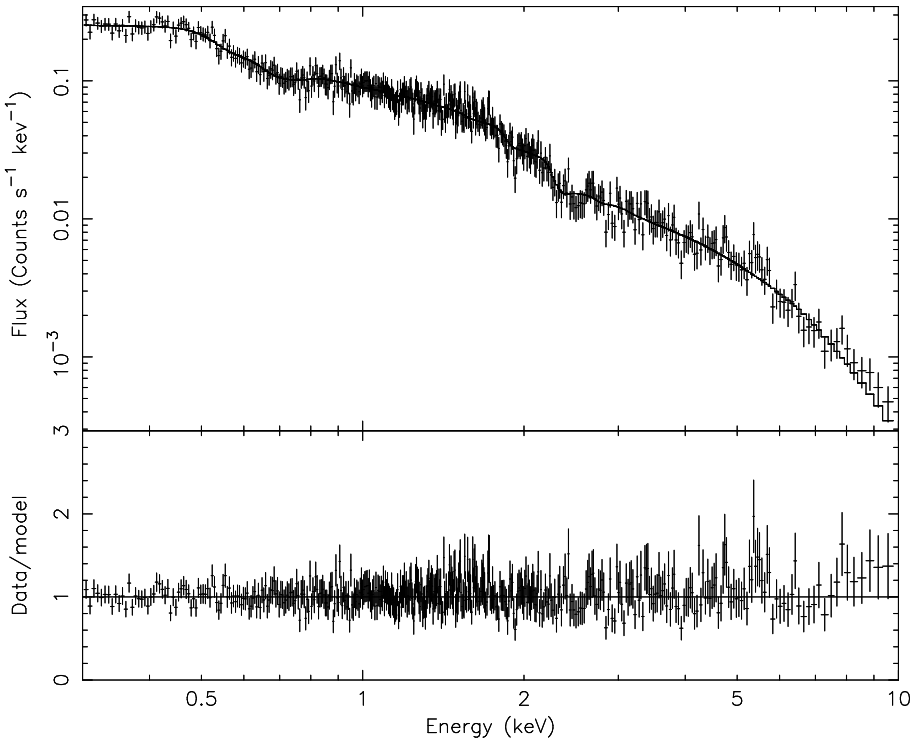

Figure 2.7: PG 1309+355: Single warm absorber fit with blackbody.

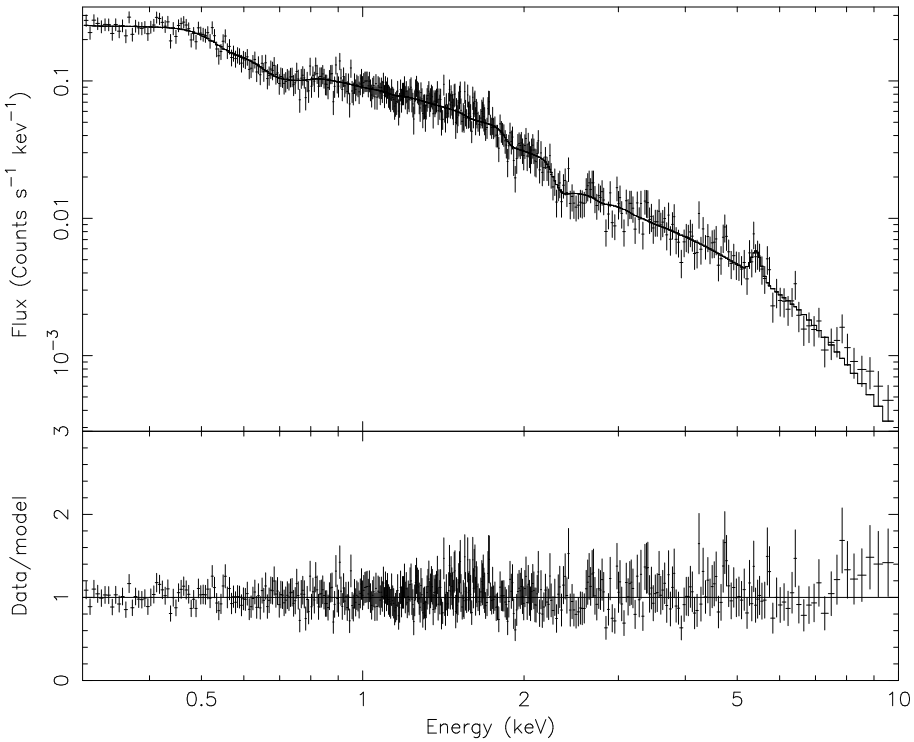

Figure 2.8: PG 1309+355: Single warm absorber fit with blackbody and iron Kα line.

Fig. 2.1 and Fig. 2.5, the data are below the power law model predicted for each quasar.

2.2.1 Models including warm absorbers

To improve the fits to the data, a warm absorber model was included in the models, as well as the power law and Galactic absorption. Each warm absorber is characterised with an ionisation parameter, ξ (Tarter, Tucker & Salpeter 1969). The ionisation parameter is defined as $\xi = L/nr^2$ in erg cm s^{-1}. Here L is the ionising X-ray luminosity (erg s^{-1}), n the gas density (cm^{-3}), and r the distance of the ionising source from the absorbing gas, in cm.

To fit the warm absorbers, I used the *xabs* model in *SPEX*, which applies line and photoelectric absorption by a column of photoionised gas. The ionisation parameters and column densities in *xabs* were allowed to vary freely, but I assumed solar elemental abundances for the ions in the absorbers.

The velocity structures of the X-ray and UV absorbers in these quasars are assumed to be the same. However, this is not necessarily true, for I show later that the absorbers could lie at different distances from the continuum source. In the models for each absorber, I used the UV absorption line outflow velocities and velocity dispersions from M98 for PG 1114+445, and from Bechtold, Dobrzycki & Wilden (2002; hereafter BO2) for PG 1309+355. The velocity dispersions were found using the relation σ = FWHM/2.35. For PG 1114+445, the outflow velocity is 530 km s^{-1} and the velocity dispersion is 213 km s^{-1}. PG 1309+355, the outflow velocity is 1500 km s^{-1} and the velocity dispersion is 247 km s^{-1}.

2.2.2 The case of PG 1114+445

Following on from the preliminary fit of Fig. 2.1, PG 1114+445 was first fitted with one warm absorber, as shown in Fig. 2.2. This improved the fit greatly, with the value of χ^2 decreasing by 3551 for 2 extra parameters. Although the fit

Table 2.2: Parameters found from the power law and warm absorber model fits for PG 1114+445 and PG 1309+355. Errors are at 90 % confidence ($\Delta\chi^2 = 2.71$). ξ is the ionisation parameter in units of erg cm s^{-1}. PL norm is the normalisation of the power law, in units of 10^{52} ph s^{-1} keV^{-1}. EW is the equivalent width of the Fe Kα line.

PG 1114+445	N_H (10^{22}cm^{-2})	log ξ	Γ	PL norm at 1 keV	Fe Kα Energy (keV)	Fe Kα FWHM (eV)	Fe Kα EW (eV)	χ^2/d.o.f
PL	—	—	1.16±0.01	2.79±0.04	—	—	—	4475/832
PL×xabs	$1.63^{+0.07}_{-0.05}$	1.50±0.03	1.77±0.02	8.28±0.24	—	—	—	924/830
PL×xabs ×xabs	$4.21^{+1.00}_{-0.70}$, 0.71±0.08	2.49±0.09, $0.88^{+0.11}_{-0.10}$	$1.87^{+0.04}_{-0.03}$	10.29±0.60	—	—	—	834/828
(PL+FeKα) ×xabs×xabs	$5.30^{+1.30}_{-1.00}$, $0.74^{+0.08}_{-0.07}$	2.57±0.08, $0.83^{+0.10}_{-0.07}$	1.92±0.04	$11.0^{+0.80}_{-0.70}$	$6.51^{+0.04}_{-0.05}$	320^{+110}_{-90}	230^{+90}_{-70}	766/825

PG 1309+355	N_H (10^{22}cm^{-2})	log ξ	BB kT (keV)	BB Area (10^{23} cm^2)	Γ	PL norm at 1 keV	Fe Kα Energy (keV)	Fe Kα FWHM (eV)	Fe Kα EW (eV)	χ^2/d.o.f
PL	—	—	—	—	1.96±0.02	4.75±0.07	—	—	—	743/456
PL×xabs	$1.00^{+0.20}_{-0.10}$	$2.03^{+0.09}_{-0.08}$	—	—	$2.08^{+0.02}_{-0.03}$	6.45±0.20	—	—	—	378/454
(PL+BB) ×xabs	$0.40^{+0.14}_{-0.12}$	1.86±0.20	0.12±0.02	$3.20^{+3.80}_{-1.50}$	1.85±0.05	4.75±0.30	—	—	—	324/453
(PL+BB +FeKα)×xabs	$0.42^{+0.14}_{-0.13}$	$1.87^{+0.10}_{-0.20}$	0.12±0.02	3.04±0.60	$1.87^{+0.06}_{-0.05}$	$4.84^{+0.40}_{-0.30}$	$6.42^{+0.12}_{-0.09}$	230^{+380}_{-230}	130^{+130}_{-80}	314/450

is much improved, from examination of the data/model ratio in Fig. 2.2, more absorption components are present than are accounted for by just one warm absorber, which in this case has a log ξ of 1.5. In the observed frame, there are some absorption features visible at $\sim$ 0.7 keV that could be due to an iron UTA, and also at $\sim$ 0.8-0.9 keV, probably due to L-shell iron. From this it is clear that the one warm absorber has too high an ionisation parameter to account for these features; this implies that another warm absorber is present.

To account for the remaining absorption features, I tried adding a second warm absorber, which improved the χ^2 by 90 for 2 additional free parameters. This is shown in Fig. 2.3. The two absorbers in the model have very different values of log ξ; the higher-ξ absorber has a log ξ of 2.49, and N_H of 4.2×10^{22} cm^{-2}, and the lower-ξ warm absorber has log ξ of 0.88 and N_H of 0.71×10^{22} cm^{-2}. The higher-ξ phase accounts for the L-shell iron, and the lower-ξ phases accounts for the iron UTA. The details of the warm absorber parameters are given in Table 2.2.

A 6.5 keV (rest-frame) iron Kα line is prominent in the spectrum. The line is incorporated into the model as shown in Fig. 2.4. I find the equivalent width of the line to be 230^{+90}_{-70} eV, whereas George et al (1997) find an equivalent width of 60^{+120}_{-60} eV. With this line in the model, the parameters of the warm absorbers do not change significantly; the higher-ξ absorber has log ξ of 2.57, $N_H = 5.3\times10^{22}$ cm^{-2}, and the low-ξ absorber has log ξ of 0.83, $N_H = 0.74\times10^{22}$ cm^{-2}. We take the fit shown in Fig. 2.4 to be the best-fit model. The confidence intervals on the ranges of ξ and column density for this fit are shown in Fig. 2.9 and Fig. 2.10 for PG 1114+445.

The 0.3-10 keV flux of the final model is 3.1×10^{-12} erg s^{-1} cm^{-2}, compared to 1.7×10^{-12} erg s^{-1} cm^{-2} (estimated using PIMMS) from the *ASCA* observation of George et al (1997). The 1-1000 Rydberg luminosity of the final model is 4.5×10^{44} erg s^{-1}.

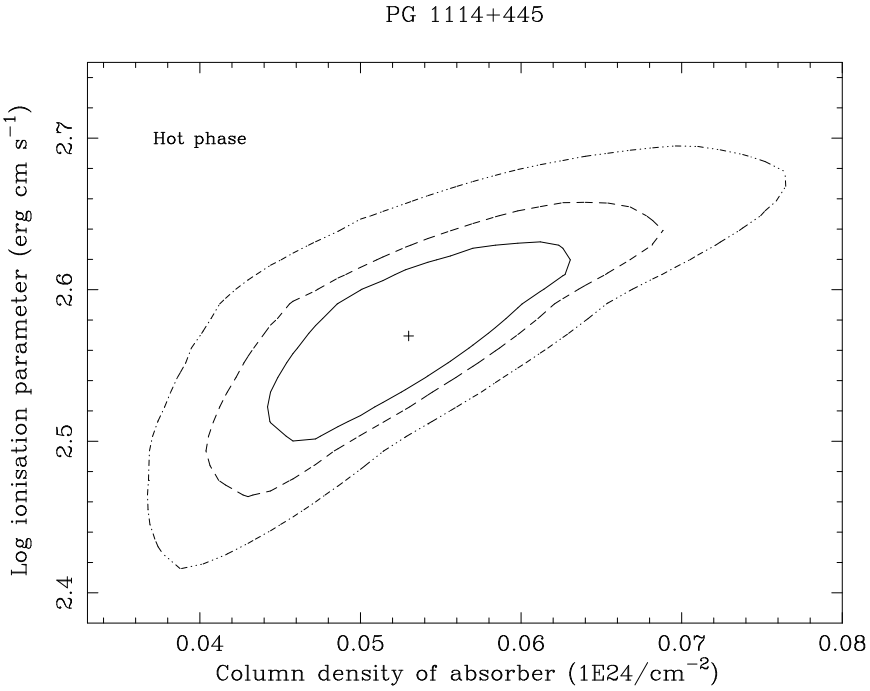

Figure 2.9: Confidence contours for the higher-ξ absorber in PG 1114+445

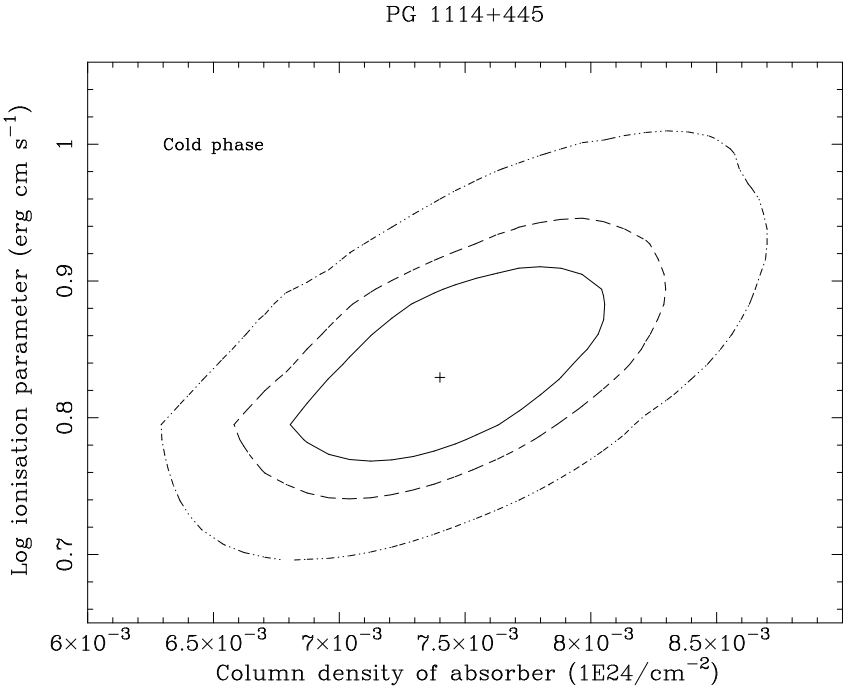

Figure 2.10: Confidence contours for the lower-ξ absorber in PG 1114+445

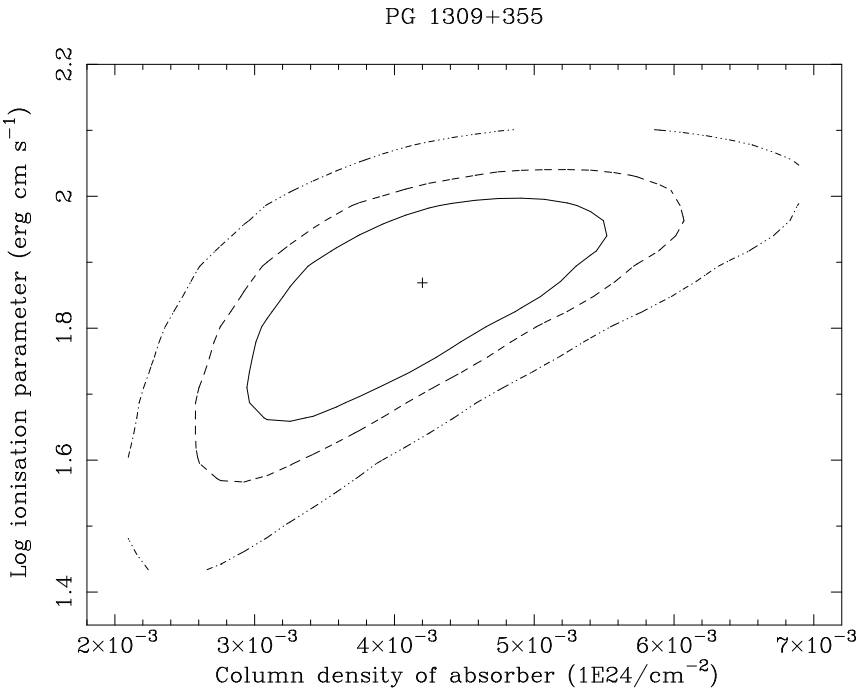

Figure 2.11: Confidence contours for the absorber in PG 1309+355

2.2.3 The case of PG 1309+355

A power law and a single warm absorber are a reasonable fit for PG 1309+355, as shown in Fig. 2.6; from the data/model ratio, the fit is much improved. A better fit still was obtained when a soft excess blackbody component was added to the model, which reduced the χ^2 by 54 for 2 extra free parameters. This fit is shown in Fig. 2.7.

An iron Kα line at 6.4 keV (rest-frame), with equivalent width 130^{+130}_{-80} eV, is detected, and included in the model in Fig. 2.8. All fits parameters are given in Table 2.2. The best-fitting model has $\log \xi = 1.87$, and a blackbody temperature of 0.12 keV. The confidence intervals for $\log \xi$ and column density for the best fit are shown in Fig. 2.11. The 0.3-10 keV flux of the final model is 1.3×10^{-12} erg s^{-1} cm^{-2}, and the 1-1000 Rydberg luminosity of the final model is 2.2×10^{44} erg s^{-1}.

2.3 Discussion

Useful physical constraints have been found for the warm absorbers in the quasars PG 1114+445 and PG 1309+355, from a detailed analysis. In order to determine the main absorbing species and see how they compare with warm absorbers observed in other AGN, the best-fitting models are plotted at a resolution higher than that of *EPIC*, in Fig. 2.12. The main ionic species contributing to the warm absorption in each AGN are labelled. These models do not include Galactic absorption, and are shown in the rest frames of the AGN.

For PG 1114+445, the most important ions in the cold phase are O V-VII, and Fe XI-XIII. The iron UTA, an indication of a low-ξ phase in a warm absorber, is very prominent in the model of PG 1114+445; the UTA consists of iron ions towards the top of the M-shell range, encompassing Fe IX-XIV. The high-ξ phase is dominated by the ions O VIII and Fe XVIII-XXII. The absorber in PG 1309+355 is too highly ionised for there to be an iron UTA; the most important ions in the single phase absorber of this quasar are O VII-VIII and Fe XIII-XVIII.

Porquet et al (2004) model *EPIC* data of PG 1114+445 and PG 1309+355 with simple absorption edges of O VII and O VIII. For PG 1114+445, they obtain optical depths of $2.26^{+0.22}_{-0.19}$ for the OVII edge, and 0.32 ± 0.16 for the OVIII edge. For PG 1309+355 they obtain $0.46^{+0.20}_{-0.15}$ for the OVII edge, and < 0.25 for the OVIII edge.

Converting from the optical depth values of Porquet et al (2004), for the warm absorber of PG 1114+445, assuming a single phase of absorption we find that the optical depths correspond to an equivalent hydrogen column of 2×10^{22} cm^{-2}. Similarly, for PG 1309+355, the optical depth corresponds to an equivalent hydrogen column density of 7×10^{21} cm^{-2}.

From our detailed fitting, we obtain columns of 5.3×10^{22} cm^{-2} and 7.4×10^{21} cm^{-2} for the two absorbers in PG 1114+445, and 4.2×10^{21} cm^{-2} for the single

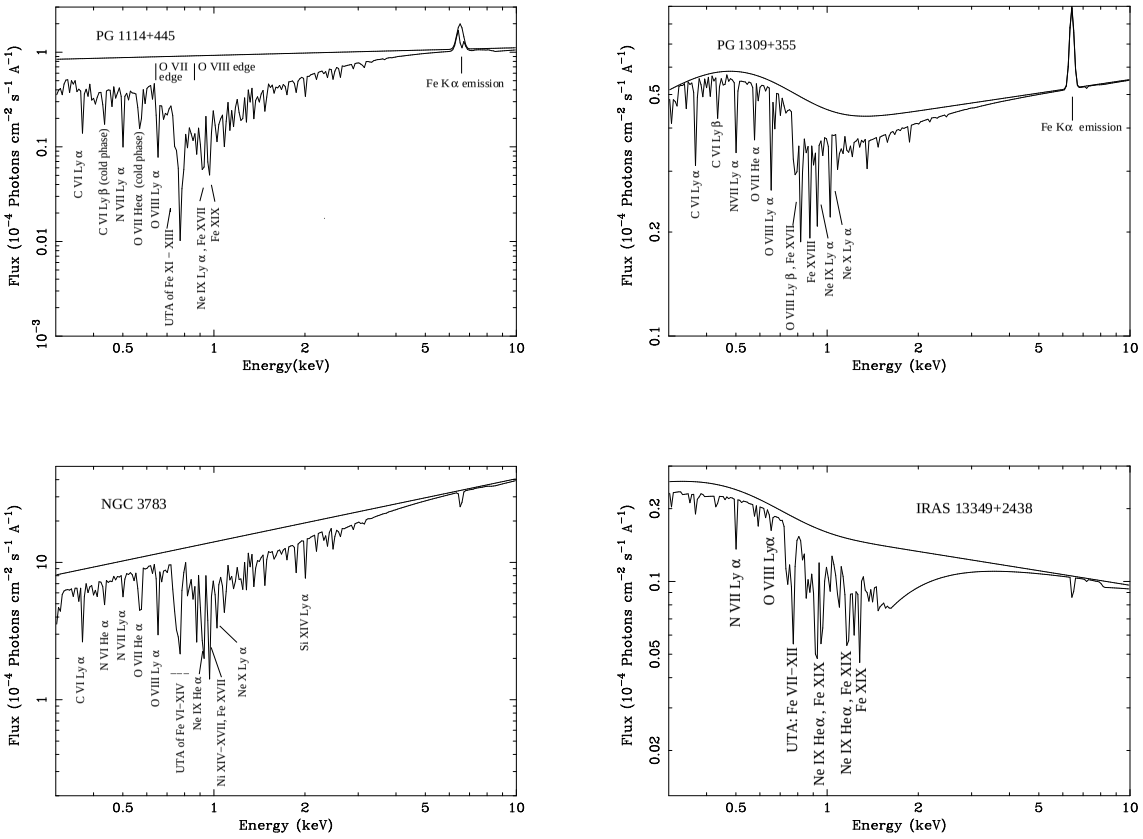

Figure 2.12: Models of the warm absorbers plotted at high resolution, in the rest frame. The dominant ions are labelled. Clockwise from top left: PG 1114+445, PG 1309+355, IRAS 13349+2438 (Sako et al 2001), NGC 3783 (Blustin et al 2002). For comparison, the solid lines show the models with no ionised absorption.

absorber PG 1309+355; these are the same order of magnitude as the converted values of Porquet et al (2004), again taking into account the estimation uncertainties.

2.3.1 Distances, filling factors and densities of the absorbers

The locations of warm absorbers in the geometry of AGNs have yet to be well constrained; the distance, r, to the warm absorber from the continuum source has been speculated to range from 10^{17} to 10^{19} cm (Krolik & Kriss 2001). However, we can put constraints on where we believe the absorbers lie.

Assuming $\delta r/r \leq 1$, i.e. the depth of the absorber, δr, cannot be greater than its distance from the source, using the relation $\xi = L/nr^2$ for the ionisation parameter, and taking $\mathrm{N_H} = n\delta r f$, where f is the filling factor of the gas and $\mathrm{N_H}$ the column density of the absorber, then

$$r \leq \frac{Lf}{\mathrm{N_H}\xi} \tag{2.1}$$

I assume the conservative upper limit of $f \leq 1$. Upper limits can then be found for the distances from the continuum source to the warm absorber. This yields a distance of $\leq 3.3 \times 10^{19}$ cm to the higher-ξ absorber in PG 1114+445, and $\leq 1.2 \times 10^{22}$ cm to the lower-ξ absorber. For PG 1309+355, the upper limit on the absorber distance is $1.6{\times}10^{21}$ cm.

Assuming that the outflow velocity, $v_{outflow}$, derived from the UV data, exceeds the escape velocity, which is defined as

$$v_{escape} = \sqrt{\frac{2GM}{r}} \tag{2.2}$$

where M is the black hole mass and G the gravitational constant, then a lower limit, r_{min}, can be found for the distance from the absorber to the continuum source:

$$r \geq r_{min} = \frac{2GM}{v^2_{outflow}} \tag{2.3}$$

Using the black hole masses given in Table 2.4, I find that $r \geq 2.4 \times 10^{19}$ cm for PG 1114+445. Similarly, for PG 1309+355, I find that the minimum distance of the absorber from the continuum source is $1.9{\times}10^{18}$ cm.

Substituting r_{min} for r in equation 2.1, a lower limit can be found for the filling factor:

$$f \geq \frac{r_{min} \mathrm{N_H} \xi}{L} \tag{2.4}$$

In this way I obtain $f \geq 0.73$ for the higher-ξ absorber of PG 1114+445, and $f \geq 2.1{\times}10^{-3}$ for the lower-ξ absorber. For PG 1309+355 I find that $f \geq 1.2{\times}10^{-3}$.

To compute lower limits on the gas density for each absorber phase, I use the relation $n = \mathrm{N_H}/\delta r f$ with δr equal to the maximum value of r, $f = 1$ and $\mathrm{N_H}$ equal to the lower limit found in the fit. For PG 1114+445, I find $n \geq 1300$ cm^{-3} for the higher-ξ phase, and $n \geq 0.60$ cm^{-3} for the lower-ξ phase. I obtain a limit of $n \geq 1.8$ cm^{-3} for PG 1309+355.

It is possible that in PG 1114+445 there is a range of log ξ in the absorber, instead of two discrete clouds. The log ξ values in the best-fitting model would then reflect the dominant ionisation states within the warm absorber. A range of log ξ has been observed in the absorbers of several objects, e.g. NGC 3783 (Blustin et al 2002); NGC 5548 (Steenbrugge et al 2003); IRAS 13349+2438 (Sako et al 2001).

2.3.2 Outflow and accretion rates

In order to investigate the dynamics of the quasars, the mass outflow rate, $\dot{M}_{out}$, was calculated. Assuming a spherical outflow, I obtain:

$$\dot{M}_{out} = 4\pi v m_p n r^2 \tag{2.5}$$

where v is the outflow velocity, m_p is the proton mass, n is the density and r is the absorber distance from the continuum source. I assume the velocity derived from the UV data for the outflow velocity. Substituting $\xi = L/nr^2$ into equation 2.5,

I derive:

$$\dot{M}_{out} = \frac{\Omega v m_p L f}{\xi} \tag{2.6}$$

where 4π is replaced by Ω, the solid angle subtended by the outflow, and f is the filling factor. I assume the warm absorber fills all lines of sight not blocked by the molecular torus, and therefore take the solid angle of the warm absorber to be $0.2\times4\pi$, based on the observed ratio of Seyfert 1s to Seyfert 2s (Maiolino & Rieke 1995).

For the hot phase in PG 1114+445, I calculate that 2.6 $M_\odot$ yr^{-1} $\leq \dot{M}_{out} \leq$ 5.1$M_\odot$yr^{-1}, and in the cold phase, 0.4 $M_\odot$ yr^{-1} $\leq \dot{M}_{out} \leq$ 270$M_\odot$ yr^{-1}. For PG 1309+355 I calculate a mass outflow of 0.02 $M_\odot$ yr^{-1} $\leq \dot{M}_{out} \leq$ 47$M_\odot$ yr^{-1}. These mass outflows for the absorbers can be compared with the mass accretion rates for each quasar,

$$\dot{M}_{acc} = \frac{L_{bol}}{\eta c^2} \tag{2.7}$$

where L_{bol} is the bolometric luminosity, c is the speed of light, and η is the accretion efficiency, which I assume to be 0.1. For PG 1114+445, $L_{bol} = 5 \times 10^{45}$ erg s^{-1} (M98), and for PG 1309+355, $L_{bol} = 6.8 \times 10^{45}$ erg s^{-1} (Laor 1998). For PG 1114+445, I obtain a mass accretion rate of 0.9 $M_\odot$ yr^{-1}. Therefore, the outflow appears to be larger than the accretion rate in PG 1114+445. The accretion rate of PG 1309+355 is 1.2 $M_\odot$ yr^{-1}.

The kinetic luminosity carried in the outflows for the absorbers was found using the relation

$$L_{KE} = \frac{\dot{M}_{out} v^2 f}{2} \tag{2.8}$$

For the higher-ξ absorber in PG 1114+445, I find 2.3×10^{41} erg s^{-1} $\leq L_{KE} \leq$ 4.5×10^{41} erg s^{-1}, while for the lower-ξ absorber, I find 3.3×10^{40} erg s^{-1} $\leq$ $L_{KE} \leq 2.5 \times 10^{43}$ erg s^{-1}; the two warm absorber phases together account for 10^{-3}-10^{-5} of the bolometric luminosity. For PG 1309+355, we find 1.5×10^{40} erg s^{-1} $\leq L_{KE} \leq 3.3 \times 10^{43}$ erg s^{-1}; so for this quasar, the kinetic luminosity of the outflow is 10^{-3}-10^{-6} times the bolometric luminosity.

2.3.3 Associated UV and X-ray absorber?

As strong evidence exists for an association between X-ray and UV absorption systems, (e.g. M98; Crenshaw et al (1999) found a one-to-one correlation of UV and X-ray absorbers in a sample of Seyfert 1 AGN), I investigated which phases of the X-ray absorber are related to the UV absorbers in the two PG quasars. I used the *SPEX xabs* model to compute the equivalent widths of the UV absorption lines, due to the warm absorbers modelled in the X-ray data. These are shown in Table 2.3.

The UV lines observed by M98 all appear in the low-ξ phase model of PG 1114+445, with comparable equivalent widths, so I identify the UV absorber with the low-ξ X-ray absorber phase. For the low-ξ absorber, our assumption that the velocity structure is the same as that of the UV absorber is therefore justified. However, the high-ξ X-ray absorber is too highly ionised to give rise to any of the UV lines observed by M98.

For the case of PG 1309+355, the X-ray absorber is not predicted to give rise to significant C IV or N V lines, as it is too highly ionised. However, the X-ray absorber model does predict absorption from O VI at 1037 Å with an equivalent width similar to that observed. Therefore it is likely that the X-ray and UV absorbers have the same velocity structure.

2.3.4 Where is the warm absorber coming from?

In order to locate the warm absorbers in the structures of the AGN considered here, the locations of the Broad Line Region (BLR) and the torus are calculated for each quasar.

The quasars considered here are Type 1 AGN so that the observer is looking directly towards the central engine. By finding the locations of the warm absorbers relative to the BLR and the molecular torus, a useful picture of the structure of each quasar is obtained, and the origins of the warm absorbers can

Table 2.3: X-ray and UV absorber line equivalent widths in Å. B02 refers to Bechtold (2002).

Line, Å	PG 1114+445 model: $\log \xi = 0.83$	PG 1114+445 model: $\log \xi = 2.57$	PG 1114+445 observed (M98)	PG 1309+355 model: $\log \xi = 1.87$	PG 1309+355 observed (BO2)
C IV, 1548.2	5.5	—	2.4	0.02	1.63
C IV, 1550.8	4.8	—	2.1	0.01	0.43
N V, 1238.8	4.8	—	1.8	0.09	1.85
N V, 1242.8	4.4	—	1.9	0.04	1.66
O VI, 1037.6	5.2	0.06	—	1.8	1.99

be constrained.

The BLR sizes can be estimated using the empirical relation of Equation 6 in Kaspi et al (2000), derived from reverberation studies:

$$R_{\rm BLR} = (32.9^{+2.0}_{-1.9}) \left[\frac{\lambda L_\lambda (5100\text{Å})}{10^{44} \text{ergs}^{-1}} \right]^{0.700 \pm 0.033} \quad \text{lt} - \text{days} \tag{2.9}$$

In this equation, $\lambda L_\lambda(5100\text{Å})$ is the monochromatic luminosity of the continuum at 5100 Å, times this wavelength. I use $\lambda L_\lambda(5100\text{Å})$ values of 3.9×10^{44} erg s^{-1} for PG 1114+445, and 6.9×10^{44} erg s^{-1} for PG 1309+355, from Vestergaard (2002). I calculate the BLR distance in PG 1114+445 to be 2.1×10^{17} cm. I use the relation in Krolik & Kriss (2001; see also Barvainis 1987) to estimate the inner edge of the torus, in parsecs, from the ionising luminosity $L_{ion,44}$, in units of 10^{44} erg s^{-1}:

$$R_{\text{torus, pc}} \sim L^{1/2}_{ion,\ 44} \tag{2.10}$$

I estimate the torus inner edge to be 6.3×10^{18} cm for PG 1114+445. Therefore, the absorbers in this AGN are located at a much greater distance from the continuum source than the BLR, and somewhat further than the inner edge of the torus.

A similar situation exists for PG 1309+355, where the distance to the BLR is 3.3×10^{17} cm, and the torus inner edge is at 4.4×10^{18} cm. As the absorber lies further than 1.9×10^{18} cm, the warm absorber is again much further than the BLR and at least as far as the torus inner edge. Since the warm absorbers appear to lie beyond the inner edge of the torus, a torus wind is their most likely origin in these quasars. At these distances, the warm absorbers are within the narrow line region (NLR). Similarly, Sako et al (2000) suggested this was the case for IRAS 13349+2438, while in NGC 1068 the warm emitter is directly observed to be in the NLR (Ogle et al 2003, Brinkman et al 2002.)

An alternative possibility for the origin of warm absorbers is a wind launched from the accretion disk. This is modelled by Proga, Stone & Kallman (2000), who consider a disk accreting onto a 10^8 $M_\odot$ black hole. They find that the

disk radiation can launch a wind at $\sim 10^{16}$ cm from the central engine, and can accelerate it up to 15,000 km s^{-1} at an angle of $\sim$ 75 degrees to the disk axis. This can be considered for both the quasars here, which have black hole masses of $\sim 10^8$ $M_\odot$ (Vestergaard 2002). The model has a mass loss of 0.5 $M_\odot$ yr^{-1} and typical column densities generated in the wind are $\sim 10^{23}$ cm^{-2}, at least an order of magnitude higher than the warm absorbers observed in PG 1114+445 and PG 1309+355. Furthermore, the model predicts that the density of the outflow is greatest near the base of the flow, at $\sim 10^{16}$ cm, and therefore if an accretion disk wind were responsible for the warm absorbers, they would be observed at this distance from the continuum source. However, they are observed at $> 10^{18}$ cm in both quasars. Thus in the quasars considered here, the warm absorbers lie at distances too great to be produced by an accretion disk wind as described by Proga et al (2000).

There have been recent reports of high-energy outflows in the quasars PG 1211+143 (Pounds et al 2003) and PDS 456 (Reeves, O'Brien & Ward 2003), however these quasars were both found to exhibit very high ionisation parameters and high columns. PG 1211+143 was found to have log ξ of 3.4, a high column of 5 x 10^{23} cm^{-2} and an outflow of 0.12 $M_\odot$ yr^{-1} at a velocity of 0.1c. Similarly, for PDS 456, a log ξ of 2.5 and a column of 5 x 10^{23} cm^{-2} are found for a mass outflow with a rate of 10 $M_\odot$ yr^{-1} at a velocity of 0.2c. It is interesting that the log ξ of 2.5 for PDS 456 is similar to the log ξ of 2.57 found for one of the absorbers in PG 1114+445. However, the outflows in PG 1211+143 and PDS 456 are much faster than those considered in this thesis, where I have assumed justifiably, that the velocities of the X-ray absorbers are the same as those of the UV absorbers for PG 1114+445 and PG 1309+355.

2.3.5 Comparison with other AGNs

It is intriguing that the best-fitting model parameters of PG 1114+445 (L_{bol} = 5×10^{45} erg s^{-1}), shown in Table 2.2, are similar to those of NGC 3783 (L_{bol} = 4.5×10^{44} erg s^{-1}; Markowitz et al 2003), the nearest Seyfert 1 AGN with a warm absorber which has been well studied (see e.g. Kaspi et al 2002; Blustin et al 2002; Netzer et al 2003; Krongold et al 2003). In PG 1114+445, I find values of log $\xi = 2.57$, $N_H = 5.3\times10^{22}$ cm^{-2} and log $\xi = 0.83$, $N_H = 0.7\times10^{22}$ cm^{-2} for the higher- and lower-ionisation absorbers respectively. Blustin et al (2002) model NGC 3783 with two warm absorbers, a higher-ionisation one with log $\xi = 2.4$, N_H $\sim 10^{22}$ cm^{-2}, and a lower-ionisation one with log $\xi = 0.3$ and $N_H \sim 10^{20}$ cm^{-2}. PG 1114+445 is ten times higher in luminosity than NGC 3783, yet the ionisation parameters and column densities (at least for the higher ionisation phase) of their absorbers are comparable. It appears that the ionisation parameters of warm absorbers in at least some quasars are similar to those in Seyfert galaxies. George et al (1997) also noted that the warm absorber in PG 1114+445 is akin to those found in Seyfert galaxies.

Table 2.4 shows a comparison of warm absorber parameters in the two quasars studied here, along with NGC 3783 and IRAS 13349+2438. The ionisation parameters and column densities of the absorbers do not show any particular trend with luminosity. This supports the hypothesis that there is little difference in AGN warm absorber characteristics across a sizeable range in L_{bol}. From the definition of the ionisation parameter $\xi = L/nr^2$, and given that similar values of ξ are found over a large range of luminosity, I can infer, for constant density n, that r scales approximately with $L_{ion,44}^{1/2}$. Since r has the same luminosity dependance as the torus distance in Equation 2.10, this result is consistent with the warm absorber originating as a torus wind. However, the distances inferred for the warm absorbers are not sufficently constrained in Table 2.4 to be able to construct a global picture of where a warm absorber would lie in the AGN

structure, given its bolometric luminosity.

2.4 Conclusion

I have studied the warm absorbers in the quasars PG 1114+445 and PG 1309+355 using *XMM-Newton EPIC* observations. The absorption in PG 1114+445 consists of at least two phases, a 'hot' phase with a log ionisation parameter ξ of 2.57, and a 'cooler' phase with log ξ of 0.83. The most important ions in the cold phase are O V-VII and Fe XI-XIII, whilst for the high-ξ phase, the main ions are O VIII and Fe XVIII-XXII. A UTA of M-shell iron is observed in the cooler phase of the absorber. I identify the lower-ionisation absorber with that causing absorption lines in the UV spectra. This quasar exhibits absorption which is similar to that observed in the Seyfert 1 NGC 3783.

The absorption in PG 1309+355 can be modelled with a single warm absorber phase, which has log ξ of 1.87; the most important ions in this absorber are O VII-VIII and Fe XIII-XVIII.

The absorbers are located at distances of 10^{19} - 10^{22} cm from the continuum sources in these AGN; these distances suggest that the absorbers are winds from molecular tori, rather than accretion disk winds. From the definition of the ionisation parameter, the distances to the warm absorbers from the central continuum source are proportional to the square root of the AGN ionising luminosity, which is consistent with a torus wind origin. The kinetic luminosities of the outflows are insignificant compared to the bolometric luminosities of the quasars.

Table 2.4: AGN warm absorber parameters. The objects are listed in increasing order of bolometric luminosity, L_{bol}. Log ξ is the ionisation parameter. Out. vel is outflow velocity, W.A. dist. is warm absorber distance.

AGN		M_{BH} /$M_\odot$ [a]	L_{bol} [b] erg s^{-1}	log ξ erg cm s^{-1}	log N_H cm^{-2}	Out. vel km s^{-1}	W.A. dist. 10^{18} cm
NGC 3783[c]	Sy 1	9.3×10^6	2.6×10^{44}	0.3	20.73	800	0.17-42$\times10^3$
				2.4	22.45	800	0.17-6.5[g]
PG 1114+445	QSO	2.6×10^8	5.0×10^{45}	0.83	21.87	530	24.3-1$\times10^4$
				2.57	22.72	530(?)[d]	24.3-33.4
PG 1309+355	QSO	1.6×10^8	6.8×10^{45}	1.87	21.62	213	1.9-1600
IRAS 13349+2438[e]	QSO	8×10^8	8.4×10^{45}	0	21.30	420	39.0-2$\times10^5$
				2-2.5	22.40[f]	0	?[h] - 102.0[g]

[a] $M_{BH}/M_\odot$ values for NGC 3783, PG 1114+445 and PG 1309+355 from Vestergaard (2002); IRAS 13349+2438 from Brandt et al (1997).

[b] L_{bol} values for NGC 3783 from Woo & Urry (2002); PG 1114+445 from M98; PG 1309+355 from Laor (1998); IRAS 13349+2438 from Beichman et al (1980)

[c] Blustin et al (2002)

[d] The velocity of the higher-ionisation absorber is less certain, as it is not expected to contribute to the UV absorption lines.

[e] Sako et al (2001)

[f] Average columns

[g] Blustin et al (2005)

[h] Blustin et al (2005): the phase with log $\xi = 2.25$ has an outflow speed of zero, so a minimum distance cannot be found for this absorber.

Chapter 3

The Seyfert 1 AGN H 0557-385

H 0557−385 (also known as 3A 0557-383, EXO 055620-3820.2 and CTS B31.01) is a Seyfert 1 AGN at redshift 0.034 (Fairall, McHardy & Pye 1982). The Galactic neutral column density towards it is 4×10^{20}cm^{-2} (Dickey & Lockman 1990).

In this thesis I report the first observations of this source with *XMM-Newton*. H 0557-385 has also been observed with *ASCA* (Turner et al 1996) and *BeppoSAX* (Quadrelli et al 2003). Both previous observations detected a warm absorber. In this work I explore the details of the warm absorption in H 0557-385, using both EPIC and RGS data.

H 0557−385 was observed with *XMM-Newton* (Jansen et al 2001) on 3rd April 2002 and 17th September 2002; the observation details are summarised in Table 3.1.

The EPIC pn data were taken in large window mode, and the MOS data in small window mode, both using the thin filter. Periods of high background, identified in 5-10 keV lightcurves for the whole field of view outside the source region, were excluded. The data were processed using the Science Analysis System (SAS) Version 6; the pn spectra were accumulated using single and double events, corresponding to PATTERN values of 0-4, and the MOS spectra were constructed using all valid events (PATTERN = 0-12). The count rates are below the thresholds where pile-up has to be considered (12 counts s^{-1} for the pn

Table 3.1: Observation details. The RGS count rates are for the co-added first and second orders of RGS1 and RGS2, for each observation. The Effective Exposure Time is the exposure time with periods of high background excluded.

Date Observed	Effective Exposure Time (ks)	Background-subtracted Count Rate (Counts s^{-1})
03.04.2002	pn: 8, MOS: 3, RGS: 12	pn: 10.29±0.05, MOS1: 3.30±0.04, MOS2: 3.32±0.04 RGS:0.125±3 $\times 10^{-3}$
17.09.2002	pn: 7, MOS: 9, RGS: 8	pn: 10.55±0.04, MOS1: 3.63±0.02 MOS2: 3.68±0.02 RGS:0.143±3 $\times 10^{-3}$

large window mode, and 5 counts s^{-1} for the MOS small window mode). Events next to bad pixels and next to the edges of CCDs were excluded (FLAG = 0 in SAS).

The EPIC source spectra were constructed by selecting counts within a circle of radius 25 arcsec, and the background spectra were extracted from nearby source-free regions in circles of radius 75 arcsec.

Response matrix files (RMF) and auxiliary response files (ARF) for each instrument were generated using the *SAS*. The count rates for each observation are similar, as shown in Table. 3.1. The EPIC spectra from both observations were coadded using the method of Page, Davis & Salvi (2003) and binned into 45 eV channels.

The RGS spectra were extracted using *rgsproc* in SAS V.6. The first and second order spectra and response matrices from both RGSs and both observations were resampled to the channels of the first order RGS1 spectrum from April 2002. The spectra were then coadded, and the response matrices were combined,

to produce a single spectrum and a single response matrix. The spectrum was then binned by a factor of 9 to improve signal to noise, giving a binsize of 0.1 Å at 20 Å. The data were analysed using *SPEX* 2.00 (Kaastra et al 2002). I adopt a cosmology with $H_0 = 70.0$ km s^{-1} Mpc^{-1}, $\Omega_m = 0.3$ and $\Omega_\lambda = 0.7$.

3.1 Fits to the EPIC data

The combined *pn* and *MOS* data were fitted in *SPEX* with a number of spectral models: the fit parameters are listed in Table 3.2. Figs. 3.1-3.6 show the spectra and data/model ratios for the combined *pn* and *MOS* data. All spectra are plotted in the observed frame, unless otherwise stated.

Absorption by the Galactic column density is included in all the fits, using the model *hot*, in *SPEX*. This is for a gas in collisional ionisation equilibrium, set at the minimum temperature (5×10^{-4} keV), and it produces a very similar spectrum to that of a pure photoelectric model (e.g. Morrison & McCammon 1983), but includes absorption lines as well as absorption edges.

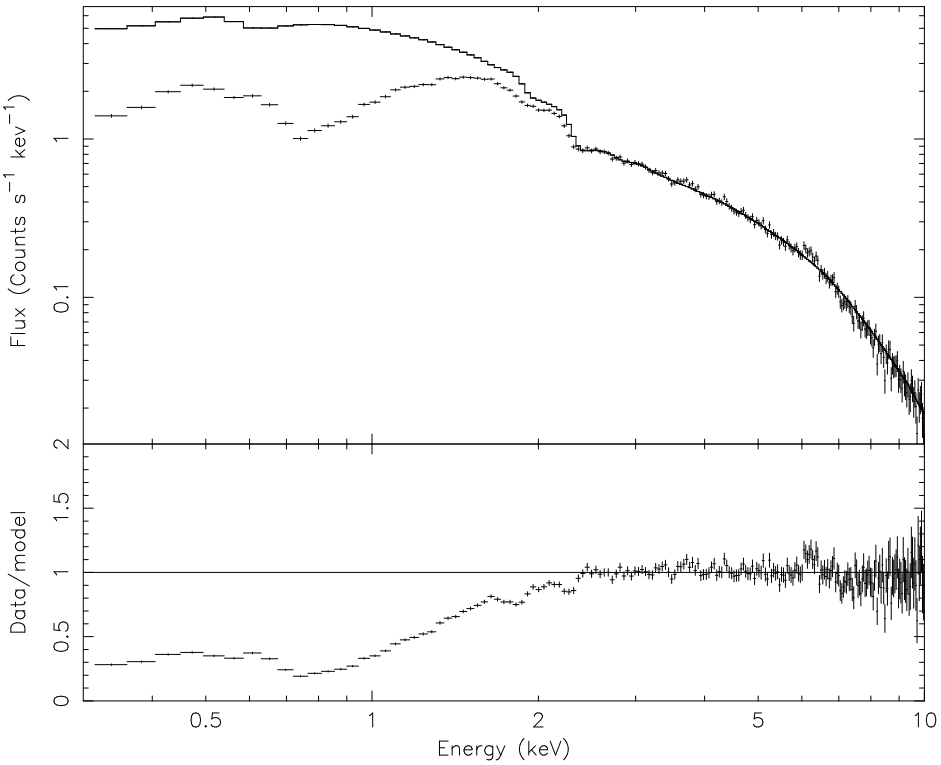

Figure 3.1: Power law fit (Model A).

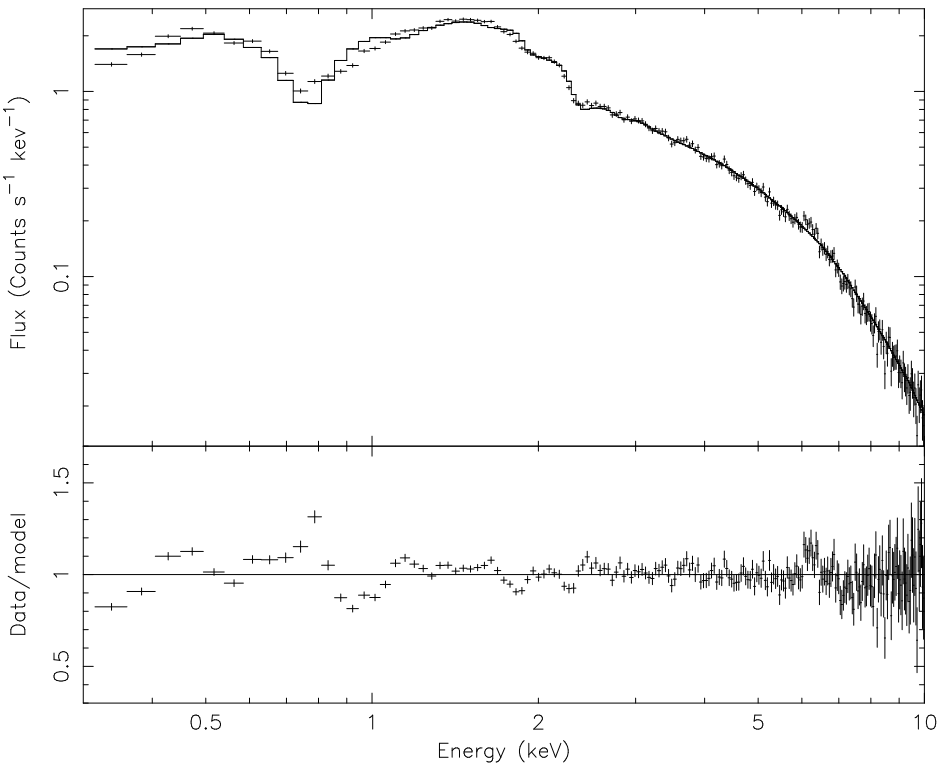

Figure 3.2: Fit with one warm absorber (Model B).

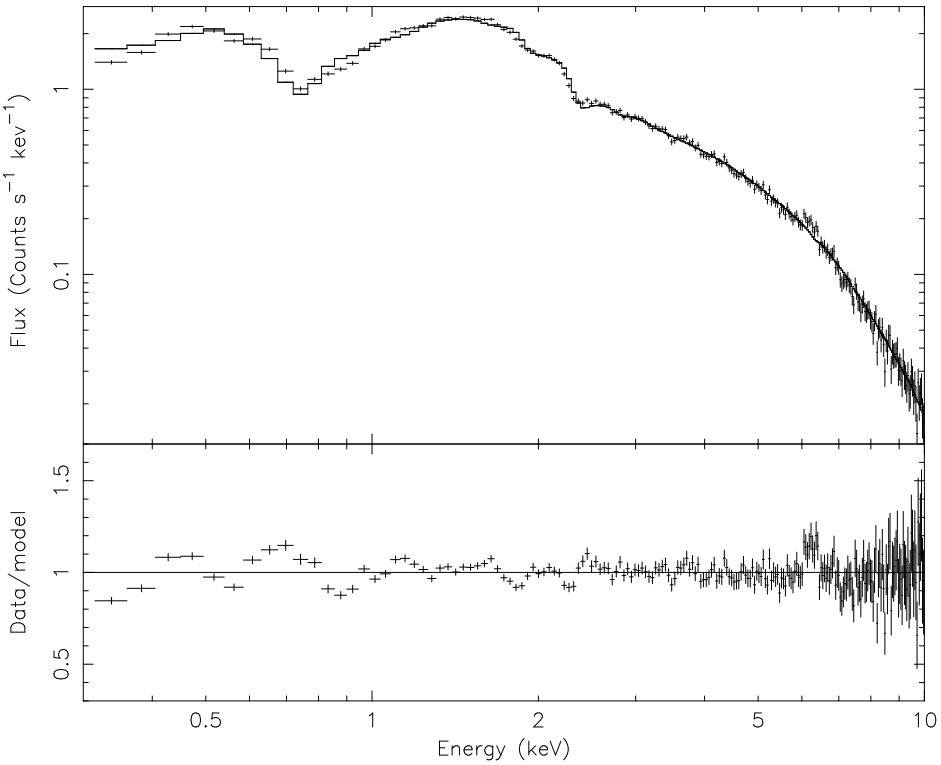

Figure 3.3: Fit with two warm absorbers (Model C).

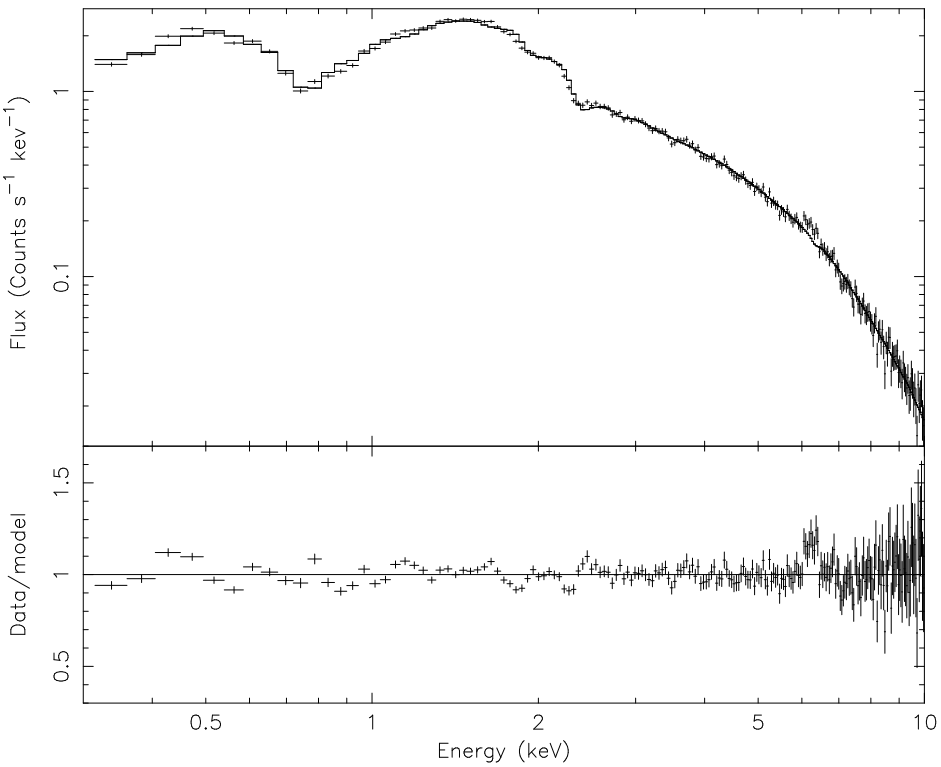

Figure 3.4: Fit with two warm absorbers and neutral absorption (Model D).

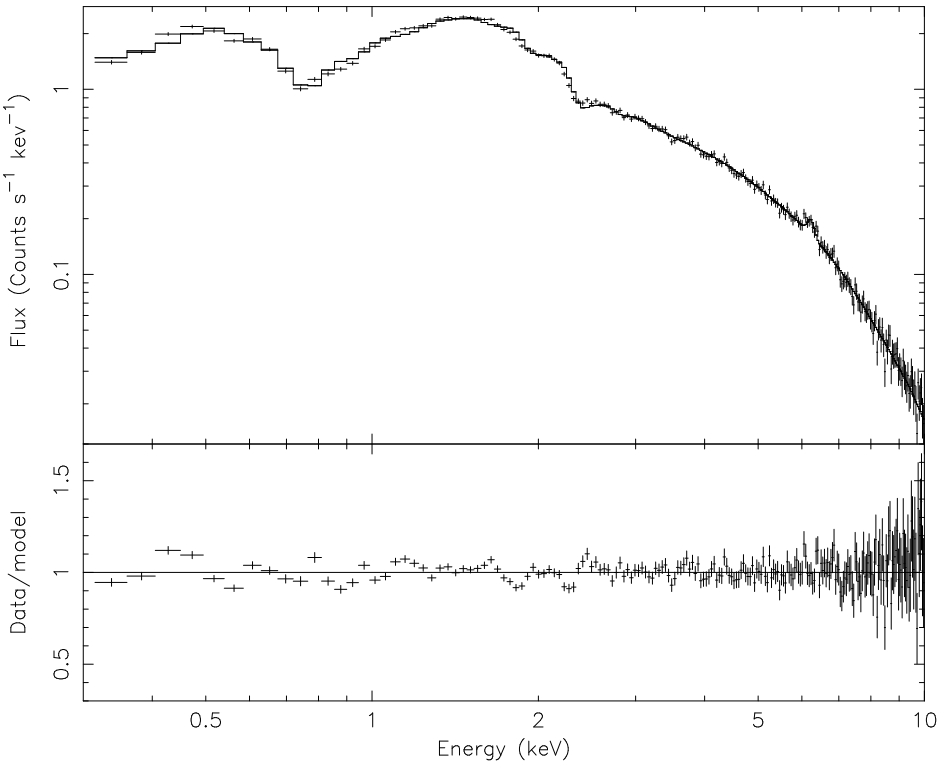

Figure 3.5: Fit with two warm absorbers, neutral absorption and iron Kα line (Model E).

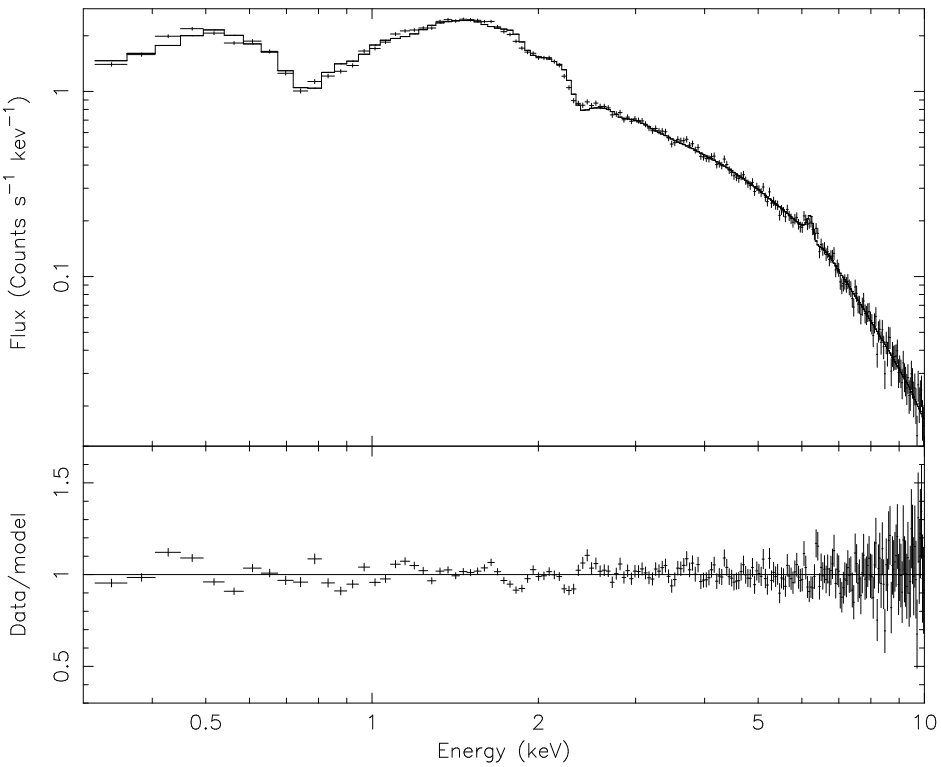

Figure 3.6: Fit with two warm absorbers, neutral absorption and reflection (Model F).

I started by fitting a simple power law in the range 2.3-10 keV (Model A) to avoid the regions where the low-energy absorption affects the spectrum. In Fig. 3.1 the power law is plotted back to 0.3 keV to show the shape and extent of the absorption. The plot is suggestive of the presence of a warm absorber, with the deepest trough occuring at $\sim$ 0.7 keV; at this energy this will be a warm, rather than a neutral absorber.

To fit the whole spectrum, a warm absorber component (*xabs* in *SPEX*) was added to the model (Model B). The *xabs* component models absorption by a cloud of photoionised gas, at a given column and ionisation parameter, where the ionisation parameter is defined as $\xi = L/nr^2$ in erg cm s^{-1}. As mentioned previously, L is the 1-1000 Rydberg ionising luminosity (erg s^{-1}), n the gas density (cm^{-3}), and r the distance of the ionising source from the absorbing gas, in cm. The turbulent velocity of the gas is set to 100 km s^{-1}, and the elemental abundances to solar values. Only the column and ionisation parameter were left free in the fitting.

Including the warm absorber in the model brings it to resemble the data far more closely, as shown in the plot for Model B. However, the χ^2/dof is 946/211, and the model is still not a good match to the data at some energies. The single *xabs* component has created an absorption feature in the model which is deeper than that in the data at $\sim$ 0.75 keV, but the model has insufficent absorption at 1 keV, as examination of the data/model ratio in Fig. 3.2 shows.

Another *xabs* component with a much higher ionisation parameter was added (Model C): this reduces the ionisation parameter and column of the first *xabs* component and provides a better fit to the data at $\sim$ 0.75 keV and 1 keV, as shown in Fig. 3.3. The goodness of fit is significantly improved, but the model still appears to require some absorption at $\sim$ 0.3-0.4 keV to match the data. Therefore a component of neutral gas (again, using *hot* in *SPEX* at the minimum temperature of 5×10^{-4} keV) was added at the same redshift as H 0557−385. The column density of neutral gas, 4×10^{20} cm^{-2}, provides a much better fit to the

Table 3.2: Parameters of fits to the combined EPIC data. The Galactic column (4×10^{20} cm^{-2}) is included in the models. PL norm is the normalisation of the power law in units of 10^{52} ph s^{-1} keV^{-1}. ξ is the ionisation parameter in units of erg cm s^{-1}. The reflection fraction is defined as $\Omega/2\pi$, where Ω is the solid angle subtended by the reflector at the X-ray source. Errors are at 90 % confidence for one interesting parameter ($\Delta\chi^2 = 2.71$). 'W.a' stands for warm absorber. The w.a and neutral N_H are in 10^{22}cm^{-2}. Refl. Frac stands for reflection fraction.

Model	Γ	PL norm at 1 keV	W.a N_H	log ξ of w.a	Neutral N_H	Fe Kα Energy (keV)	Fe Kα σ (eV)	Fe Kα EW (eV)	Refl. Frac.	χ^2/d.o.f
PL×xabs (Model B)	1.79±0.01	6.91±0.13	0.76±0.02	0.41±0.02	–	–	–	–	–	946/211
PL×xabs×xabs (Model C)	$1.83^{+0.02}_{-0.01}$	7.48±0.20	0.62±0.02 0.75±0.10	$0.07^{+0.05}_{-0.06}$ $2.25^{+0.06}_{-0.08}$	–	–	–	–	–	637/209
PL×xabs×xabs ×neutral N_H (Model D)	$1.88^{+0.02}_{-0.01}$	$8.11^{+0.25}_{-0.19}$	0.60±0.02 $1.11^{+0.26}_{-0.14}$	$0.37^{+0.05}_{-0.06}$ $2.30^{+0.07}_{-0.08}$	0.04±0.01	–	–	–	–	487/208
(PL+Fe Kα) ×xabs×xabs ×neutral N_H (Model E)	1.90±0.02	$8.37^{+0.29}_{-0.21}$	0.61±0.02 $1.27^{+0.24}_{-0.20}$	$0.36^{+0.05}_{-0.04}$ $2.33^{+0.05}_{-0.06}$	0.05±0.01	6.41±+0.05	140^{+70}_{-50}	85^{+33}_{-24}	–	438/205
(PL+refl) ×xabs×xabs ×neutral N_H (Model F)	$1.93^{+0.02}_{-0.03}$	$8.60^{+0.31}_{-0.29}$	0.61±0.02 $1.24^{+0.24}_{-0.17}$	$0.35^{+0.05}_{-0.04}$ 2.31±0.06	0.05±0.01	–	–	–	$0.39^{+0.11}_{-0.10}$	443/207

data at lower energies, as shown in Fig. 3.4 (Model D). With the addition of neutral gas, the column of the high-ξ absorber increases and the model fits the data more closely at $\sim$ 0.3-0.4 keV and $\sim$ 0.5-1 keV.

Now the soft X-ray spectrum is fitted well, I turn to the hard X-ray spectrum. An iron Kα line is visible at $\sim$ 6 keV and I first modelled it with a gaussian. This improved the χ^2 by 49 for 3 extra parameters (Model E). The energy of the line is 6.41$\pm$0.05 keV, with a FWHM of 330^{+170}_{-130} eV and equivalent width of 85^{+33}_{-24} eV. The fit is shown in Fig. 3.5. As this line may originate by fluorescence in reflecting material, I next tried a reflection model (*refl* in *SPEX*), which includes an iron Kα line, in combination with Model D. As the energy of the line indicates it comes from cold material, I assume the reflecting material is cold. The best-fit reflected fraction is $0.39^{+0.11}_{-0.10}$. The addition of this component improves the χ^2 by 44 from Model D. This is shown in Fig. 3.6, and is Model F. As the reflected fraction is small, and the addition of this component produces a slightly worse χ^2 than Model E, I conclude that the inclusion of reflection is not justified and that the iron Kα line alone is a sufficient addition to Model D. I then take Model E as the best-fit to the EPIC data.

The 2-10 keV flux of model E is $4.3\pm0.1 \times 10^{-11}$ erg s^{-1} cm^{-2}, compared to 2×10^{-11} erg s^{-1} cm^{-2} at the time of the *ASCA* observation of Turner et al (1996) and 4×10^{-11} erg s^{-1} cm^{-2} at the time of the *BeppoSax* observation of Quadrelli et al (2003). The 1-1000 Rydberg luminosity of model E is 4.3×10^{44} erg s^{-1}.

3.2 Fits to the RGS data

I now investigate the soft X-ray absorption features using the RGS, which has much higher energy resolution (E/ΔE $\sim$ 200-800) than EPIC (E/ΔE $\sim$ 20-50).

The EPIC best-fit, model E, was plotted on to the RGS spectra after convolving it with the RGS response; the result is shown in Fig. 3.7. RGS and EPIC cross-calibration shows discrepancies of up to 15 % in the band 6 Å-18 Å and

up to 10 % in $\sim$ 18 Å-36 Å (Fig 11 of Kirsch et al 2004). The spectral shape and flux of H 0557−385 are generally well reproduced, but this model does not match the RGS data completely. It overestimates the data over $\sim$ 8-15 Å and $\sim$ 23-33 Å and is too absorbed at $\sim$ 18-19 Å. In order to obtain a better fit to the RGS data, the continuum from EPIC model E was kept fixed, and the columns and ionisation parameters of the absorbers in the model were left to vary. I consider only the 8-30 Å spectrum, where RGS calibration and statistical quality of the data are best. The turbulent velocity of the gas was again set to 100 km s^{-1}. The absorbers were set at the recession velocity of the AGN. The resultant best-fit proved to be in much better agreement with the RGS data, and is shown in Fig. 3.8, along with the data/model ratio. The main ions from each absorbing phase are indicated. The parameters from the EPIC model E and RGS fits are compared in Table. 3.3.

As the RGS has better energy resolution than EPIC, the best-fit model will be closer to the real characteristics of the source. As shown in Table. 3.3, the parameters of the warm absorbers required by the RGS data are different to those from the EPIC data. With respect to the EPIC data, for the RGS the column of the low-ξ phase is lower whereas the column of the high-ξ phase has not changed. The log ξ values of the low-ξ phase are consistent, but the log ξ of the high-ξ phase is smaller than that derived from the EPIC data. A much larger column of neutral gas is also required.

Compared to Fig. 3.7, the model in Fig. 3.8 is now a much better fit to the data at 8-15 Å and from 17 Å onwards. The χ^2/dof of the model shown in Fig. 3.7 is 413/236, whereas the χ^2/dof of the RGS best-fit model (Fig. 3.8) is 246/231. The discrepancy between the data and the model at $\sim$ 18-19 Å in Fig. 3.7 has disappeared.

Fig. 3.9 shows the models corresponding to the high-ξ and low-ξ phases. The deep and broad absorption feature at $\sim$ 16-18 Å, clearly visible in the RGS spectrum, is the signature of an unresolved transition array (UTA) of M-shell

Table 3.3: Parameters of fits to the RGS data, compared with EPIC model E. Errors are at 90 % confidence ($\Delta\chi^2 = 2.71$) for one interesting parameter.

Instrument	Warm N_H ($10^{22}cm^{-2}$)	log ξ	Neutral N_H ($10^{22}cm^{-2}$)	χ^2/dof
EPIC	0.61 ± 0.02, $1.27^{+0.24}_{-0.20}$	$0.36^{+0.05}_{-0.04}$, $2.33^{+0.05}_{-0.06}$	0.05 ± 0.01	438/205
RGS	$0.20^{+0.15}_{-0.11}$, $1.30^{+0.16}_{-0.19}$	$0.50^{+0.29}_{-0.25}$, 1.62 ± 0.13	0.12 ± 0.02	246/231

iron. The log ξ values of the two phases are such that a UTA is present in both of them. There is much more absorption at shorter wavelengths for the high-ξ phase than for the low-ξ phase, as expected.

3.3 Discussion

The EPIC data broadly give the characteristics of the warm absorbers; Model E tells us that the warm absorption is caused by two phases with different ionisation parameters. A column of neutral gas is also required to explain the spectrum at $\sim$ 0.3-0.4 keV. The RGS data, at higher resolution, require a smaller log ξ value for the high-ξ phase and a smaller column for the low-ξ phase. A much larger column of neutral gas is also required for the RGS spectrum.

The Fe Kα line, with an energy of 6.41 ± 0.05 keV, originates in material that could be neutral, or ionised, up to ionisation of Fe XVIII which is consistent with this energy (Kallman et al 2004). This wide range of ionisation states corresponds to log $\xi < 2.3$, so the ionisation state of the line-emitting material cannot be well constrained. The line is well resolved in EPIC which has much better resolution than *ASCA* ($\sim$ 6600 km s^{-1} at 6.4 keV versus *ASCA*'s $\sim$ 9000 km s^{-1} for the SIS and $\sim$ 23000 km s^{-1} for the GIS). With an EPIC derived FWHM of $16{,}000^{+8000}_{-6000}$ km s^{-1}, the width of the line can be measured better than by Turner et al (1996) from the *ASCA* observation, which yielded $55{,}000^{+22{,}000}_{-24{,}000}$

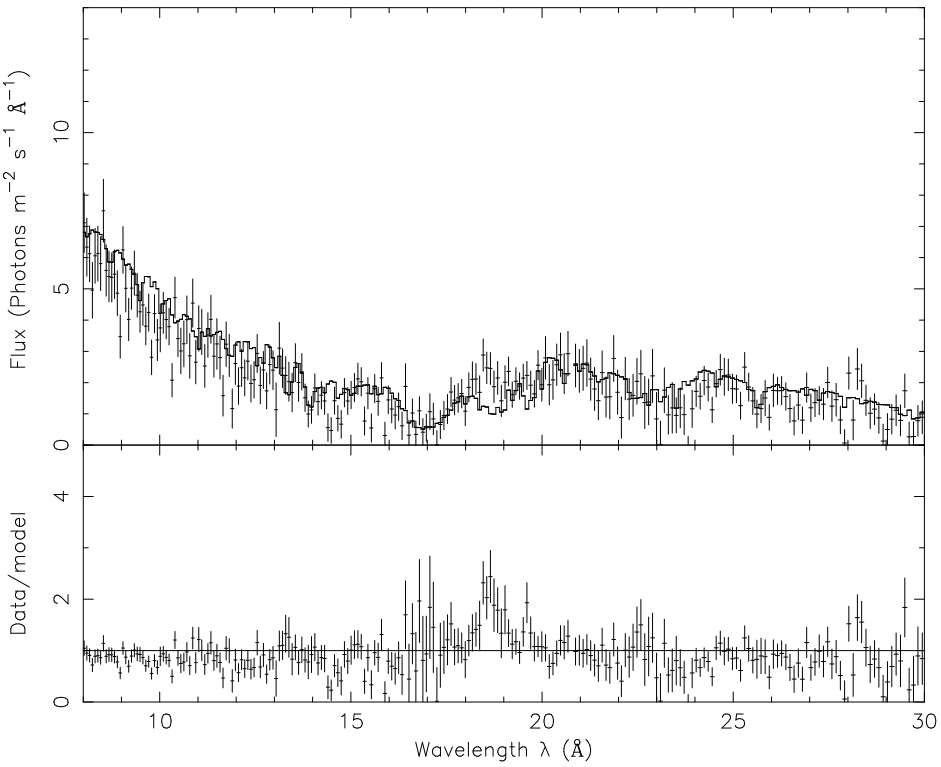

Figure 3.7: The RGS spectrum, plotted in the observed frame with the best-fit EPIC model E superimposed. The data/model ratio is also shown.

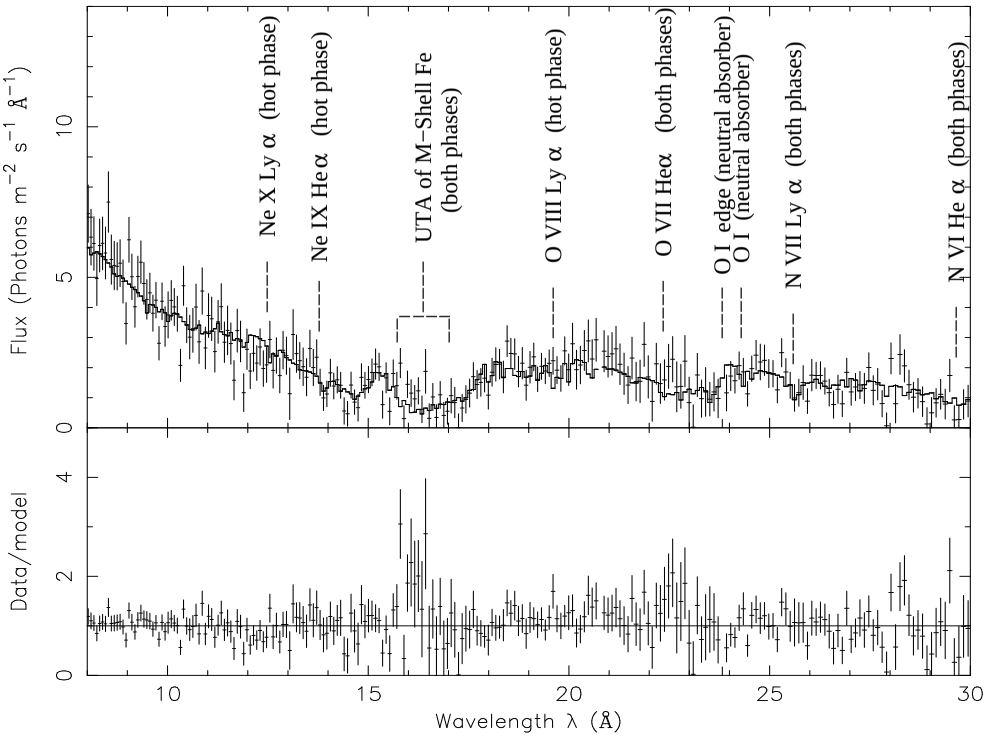

Figure 3.8: The RGS spectrum, plotted in the observed frame with the best-fit RGS model. Some of the main absorbing ions that belong to each phase are labelled. The data/model ratio is also shown.

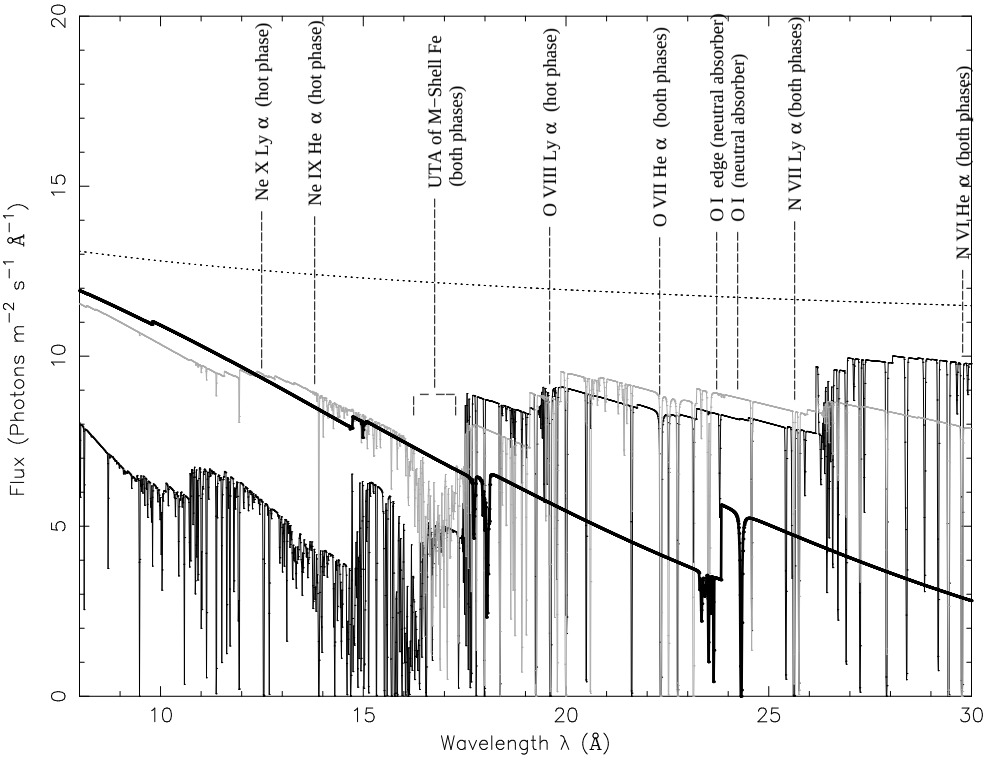

Figure 3.9: The RGS best-fit model, plotted in the observed frame, for the two absorber phases. Black: high-ξ phase. Grey: low-ξ phase. The top dotted curve, shown in black, is the unabsorbed continuum; the lower curve, also in black, includes the neutral gas. The Galactic column is not included in any of the models in this plot.

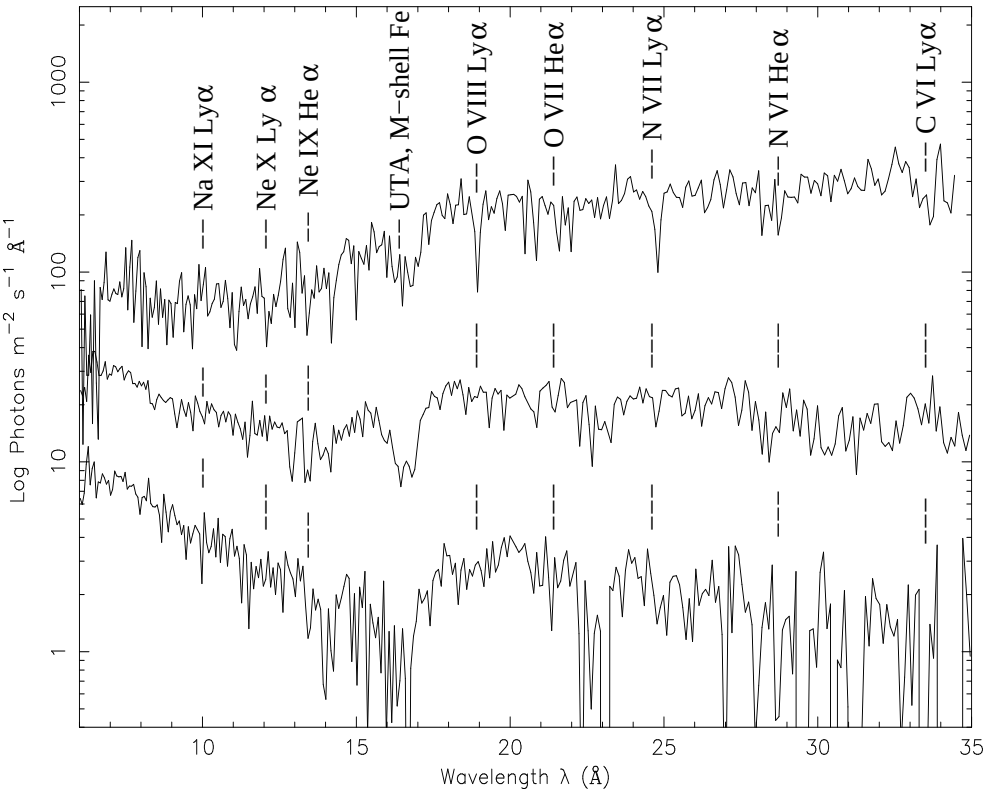

Figure 3.10: IRAS 13349+2438, upper spectrum, NGC 3783, middle spectrum, and H 0557−385, lower spectrum, all corrected for Galactic column and plotted in the rest frame. IRAS 13349+2438 has been scaled up by a factor of 80, and NGC 3783 has been scaled up by a factor of 3. The errors are not included for clarity. Some of the main absorbing ions are labelled.

km s^{-1}. I find the equivalent width of the line to be 85^{+33}_{-24} eV, compared with $\sim$ 300 eV found by Turner et al (1996).

From optical spectroscopy, Rodríguez-Ardila et al (2000) distinguish 3 Hα components in H 0557−385. The FWHM of the narrowest component is 1035 km s^{-1}, that of the intermediate component is 2772 km s^{-1} and for the broadest component it is 11,000 km s^{-1}. The last value suggests that the region that produces the broadest Hα component could also be the location of the Fe Kα line emitting gas.

To start to build up a picture of the AGN as a whole, I use the relation in Krolik & Kriss (2001) to estimate the approximate distance to the inner edge of the torus, R_{torus}, in cm, from the continuum source with ionising luminosity L, in erg s^{-1}:

$$R_{\text{torus, cm}} \sim 3 \times 10^{-4}\sqrt{L} \tag{3.1}$$

This is equivalent to Equation. 2.10 expressed in cgs units. Using the 1-1000 Rydberg luminosity from the EPIC best-fit model, i.e. $L = 4.3{\times}10^{44}$ erg s^{-1}, I obtain $6.2{\times}10^{18}$ cm ($\sim$ 2 pc) for the inner radius of the torus.

To place a distance on the Fe Kα line formation region from the black hole, I use a black hole mass of $3{\times}10^{7}$ M$_{\odot}$. This value is intermediate to the Schwarzchild and Kerr black hole masses measured for H 0557−385 by Rokaki & Boisson (1999), who assume that Hβ emission lines come from the disk. I use the FWHM of 16,000 km s^{-1} of the Fe Kα line as v in the equation:

$$v = \sqrt{\frac{GM}{R}} \tag{3.2}$$

to obtain the distance, R, of the line formation region from the black hole, assuming the line emitting gas moves in a Keplarian orbit: I obtain a distance of $2{\times}10^{15}$ cm. The Schwarzchild radius for the black hole, $2GM/c^2$, will be $9{\times}10^{12}$ cm. If I take the inner edge of the accretion disk to be $6GM/c^2$, then for H 0557−385 this is $3{\times}10^{13}$ cm. For the Hα line I find distances of $4{\times}10^{17}$ cm, $5{\times}10^{16}$ cm, and $3{\times}10^{15}$ cm for the narrowest, intermediate and broadest components respectively.

The distance of the broadest Hα line is very close to that of the Fe Kα line, which suggests that these lines both come from the same place.

3.3.1 Where did the warm absorbers originate?

I now try to determine the distances of the warm absorbers from the continuum source, and thus find some clue as to their origins.

I assume the warm absorbers to be a continous, constant velocity wind. I use R_l as the launching radius of the wind; for such a wind, $N_H = n_l R_l f$ and $\xi = L/n_l R_l^2$. L is the 1-1000 Rydberg luminosity (4.3×10^{44} erg s^{-1} from the EPIC best-fit model), n_l is the density at R_l and f is the volume filling factor of the gas. Substituting to eliminate n_l, I obtain

$$L = \frac{\xi N_H R_l}{f} \tag{3.3}$$

Taking the upper limit of the volume filling factor, $f = 1$, and including the 90 per cent confidence limits on the other parameters, I obtain upper limits of $R_l \leq 1\times10^{21}$ cm to the higher-ξ absorber, and $R_l \leq 2\times10^{23}$ cm to the lower-ξ absorber. Unfortunately, the locations of the warm absorbers cannot be constrained any better from the data available.

3.3.2 Comparison with other AGN

NGC 3783 and IRAS 13349+2438 are AGN with warm absorbers that display significant UTAs, similar to H 0557−385. A comparison of their RGS spectra, corrected for redshift and Galactic column, is shown in Fig. 3.10, and the parameters of the warm absorbers observed in these AGN are listed in Table 3.4.

The warm absorbers of these three AGN exist in multiple phases and are parameterised as two phases from the RGS observations. More recently, Netzer et al (2003) conducted a more detailed study into NGC 3783 using *Chandra* data, finding that the warm absorption exists in three phases, that correspond

Table 3.4: Comparison of warm absorber parameters for the type 1 AGN NGC 3783, IRAS 13349+243 and H 0557−385.

AGN	N_H ($10^{22}cm^{-2}$)	log ξ
NGC 3783[a]	$0.054^{+1\times10^{-3}}_{-5\times10^{-3}}$, $2.8^{+0.0}_{-0.3}$	0.3, 2.4
IRAS 13349+2438[b]	0.2±0.1, 2.5±1.5	0, 2.25
H 0557−385	$0.20^{+0.15}_{-0.11}$, $1.30^{+0.16}_{-0.19}$	$0.50^{+0.29}_{-0.25}$, 1.62±0.13

[a] Blustin et al (2002) [b] Sako et al (2001)

to log ξ values of 1.1, 2.3 and 2.9; however the RGS derived parameters of these AGN are directly compared for consistency. From the RGS observation, the warm absorbers of NGC 3783 have a combined log N_H value of 22.5, and those of IRAS 13349+2438 have a combined log N_H of 22.4. H 0557−385 is more heavily absorbed than the other two; it has a combined log N_H of 22.2, but also has an intrinsic neutral gas component, which absorbs it particularly at longer wavelengths, although this component has a much smaller column (log N_H of 21.1).

In H 0557−385 the ionisation parameters of the two phases are such that the UTA is produced in both, but in NGC 3783 and IRAS 13349+2438 the UTA only comes from the lower-ξ phase. The column of the lower-ξ phase in NGC 3783 is much smaller than the lower-ξ phase columns in the other two AGN; however, in the spectral fitting of Blustin et al (2002), it was found that iron needs to be overabundant by a factor of ~ 10 with respect to C, N and O in order to account for the depth of the UTA, so the column for the low-ξ phase should effectively be considered as ten times higher than that listed in Table 3.4.

3.3.3 Where is the neutral gas component?

I find that the RGS data of H 0557−385 require absorption from neutral gas local to the galaxy, of density $1.20\times10^{21}\mathrm{cm}^{-2}$. But where is this gas in the AGN structure? Fairall, McHardy & Pye (1982) and Rafanelli (1985) found the optical emission lines of H 0557−385 heavily reddened. Therefore if it is assumed that dust is mixed with the neutral absorber, then both must lie outside the broad line region. There are therefore three main possibilities for the location of the neutral gas: the AGN itself, the disk of the host galaxy, or somewhere in the host galaxy but outside the disk.

Scenario 1:

The first possibility is gas within the AGN itself. If the warm absorber is a wind formed by evaporation from the dusty torus, then the neutral gas could be from the torus. Ogle (2003) suggests that the torus has a role in defining the shape of the ionisation cone. As the continuum source must be viewed through the ionisation cone to see a warm absorber, we cannot be looking directly through the side of the torus. However, it could be that we are seeing cold absorption through a small cross-section of the torus if our line of sight grazes the edge.

Scenario 2:

The second possibility is the disk of the host galaxy. H 0557−385 is classified as S0a in the Nasa Extragalactic Database, between a spiral and a lenticular galaxy. It is observed at an inclination angle $i = 75°$ from the normal (Crenshaw & Kraemer 2001). If the host galaxy of H 0557−385 has similar column density values to other Sa galaxies, then the neutral absorption observed could originate in the host galaxy of the AGN. The average neutral hydrogen column density for an Sa galaxy viewed face-on, $N_{\mathrm{H}\perp}$, is 1.4×10^{21} cm^{-2} (Broeils & Woerden 1994). Using the relation $N_{\mathrm{H}} = N_{\mathrm{H}\perp}/\cos i$, I obtain an expected value of 5.3×10^{21} cm^{-2} for N_{H}. This is larger than the neutral column observed in H 0557−385, so it is

plausible the neutral gas in H 0557−385 could originate in the disk of the host galaxy.

Scenario 3:
The third possibility for the origin of this neutral gas is outside the AGN and above the disk of the galaxy, but within the structure of the galaxy. It could be in the form of a dust lane. From HST images, Malkan, Gorjian & Tam (1998) find that there are dust lanes at distances of hundreds of parsecs in Seyfert 1 and 2 AGN. These dust lanes have little or no connection with the central engine and could have column densities up to $\sim 10^{23}$ cm^{-2} (Matt et al 2000). Such a dust lane could therefore plausibly supply a column of $\sim 10^{21}$ cm^{-2}.

Given these three scenarios, I consider that all possibilities are plausible. Since some of the values of R_l (the launching radius of the wind) for different AGN in Table 4.1 are on similar scales to those of Scenario 3, it may be that the cold gas can exist on similar scales to the warm absorbers; this is plausible given the small filling factors of the warm absorbers.

3.4 Conclusion

From *XMM-Newton* RGS observations of the Seyfert 1 AGN H 0557−385 I find that warm absorption is present in two phases, a low-ξ phase with log ξ of 0.50 and a column of $\sim 10^{21}$ cm^{-2} and a high-ξ phase with log ionisation parameter ξ of 1.62 and a column of $\sim 10^{22}$ cm^{-2}. An unresolved transition array of (M-shell) iron is detected in both phases of the absorber.

I infer a picture of the different scales of these components. The locations of the warm absorbers are not well constrained ($\leq 10^{21}$-10^{23} cm from the central continuum source), compared to the molecular torus distance of $\sim 10^{18}$ cm from the source of the ionising luminosity. The Fe Kα line and a broad Hα line are both likely to originate at $\sim 10^{15}$ cm from the black hole.

From a comparison with NGC 3783 and IRAS 13349+2438, AGN with warm absorbers that also have significant UTAs similar to H 0557−385, I find that H 0557−385 is more heavily absorbed than the other two.

A column of neutral gas is observed, that could originate from the AGN torus, the host galaxy disk, or a lane or cloud of gas above the disk.

Chapter 4

Discussion

In this thesis I have examined the X-ray warm absorber outflows from two quasars, PG 1114+445 and PG 1309+355, and a Seyfert 1 AGN, H 0557−385. I will now use these results to improve our understanding of the nature and origin of warm absorbers in general.

Fig. 4.1 and Fig. 4.2 show plots of log L_{bol} versus log ξ and versus log total absorbing column for the sample of 23 AGN studied by Blustin et al (2005; hereafter B05), to which I have added (from this thesis) PG 1114+445, PG 1309+355, and H 0557−385, and also the quasar PDS 456 (Reeves et al 2003).

From these graphs, we see that PG 1114+445 and PG 1309+355 sit at the lower luminosity end of the quasars, and H 0557−385 lies at the high luminosity end of the Seyferts. The columns and ionisation parameters of all three are within the range currently observed for AGN warm absorbers. I have already pointed out in Chapter 2 that the ionisation parameters of warm absorbers in at least some quasars are similar to those in Seyfert galaxies.

4.0.1 Connection with X-ray and UV absorbers

A UV absorber was known to exist in PG 1114+445 (M98), and from my detailed study of X-ray warm absorption in this quasar, I find that the UV absorber is

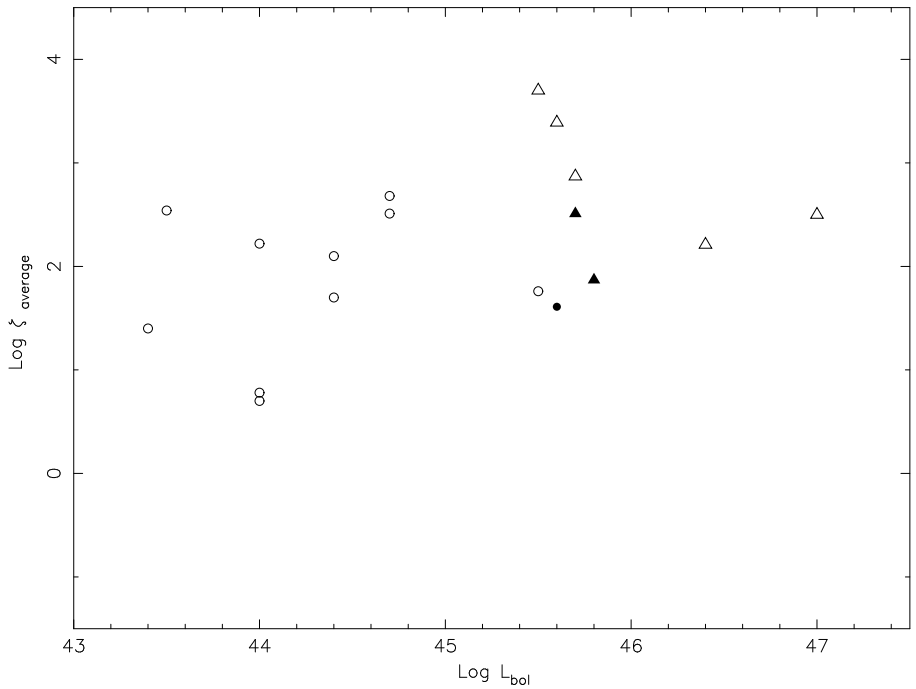

Figure 4.1: Log L_{bol} versus log ξ; updated from Blustin et al (2005). Quasars are triangles and Seyferts are circles. PG 1114+445 and PG 1309+355 are filled triangles, and H 0557−385 is a filled circle.

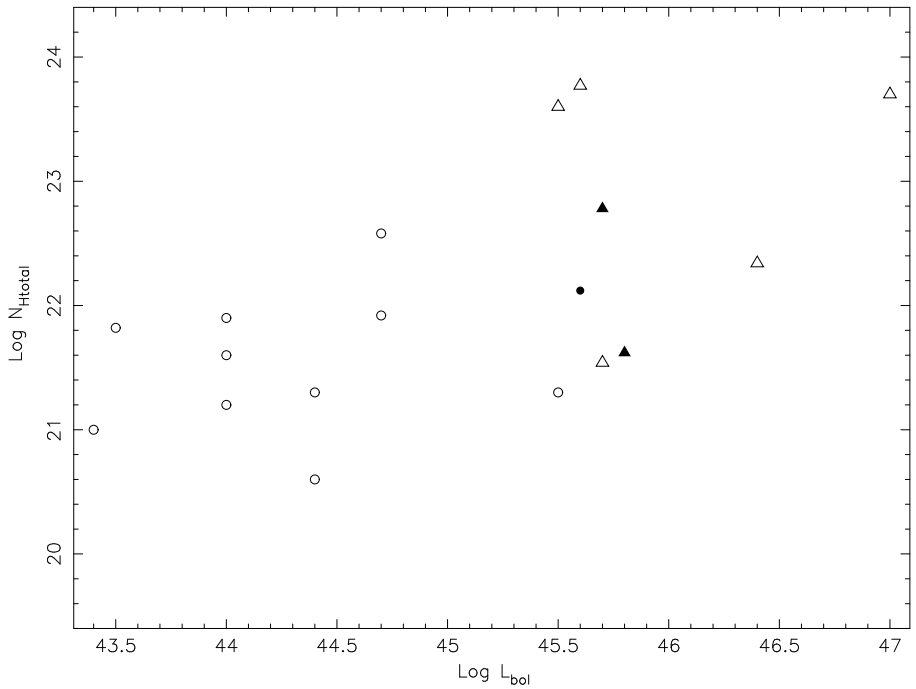

Figure 4.2: Log L_{bol} versus log N_{Htotal}; updated from Blustin et al (2005). Quasars are triangles and Seyferts are circles. PG 1114+445 and PG 1309+355 are filled triangles, and H 0557−385 is a filled circle.

associated with the lower-ξ X-ray absorber. Warm absorption had not been observed in PG 1309+355, before the *XMM-Newton* detection reported in this thesis. It is likely the X-ray absorber is associated with the UV absorber also in this source.

4.0.2 Where can we place the warm absorbers?

A crucial part of the study of warm absorbers is endeavouring to find their locations in the structure of AGNs. Whilst I am not able to find their exact locations, I can put some useful limits on them.

For PG 1114+445 and PG 1309+355, I estimate the distance range of the warm absorbers, as well as the distances of the BLR and the torus. For both AGN, the absorbers lie further out from the continuum source than the BLR, and also further out than the inner edge of the torus. This suggests that the warm absorbers in both AGN originate as a torus wind.

For H 0557−385 I can only estimate the upper distances to the absorbers; these distances include the inner edge of the torus, so a torus wind is a possibility for the origin of the absorbers in this AGN too.

4.0.3 A torus origin for warm absorbers?

Below I describe a method to determine the filling factors of warm absorbers, and I compare my findings for a sample of AGN. I then discuss the implications they have on the suggested origin of warm absorbers in torus winds.

From the relation for the ionisation parameter, $\xi = L/nr^2$, I infer that for constant density and ξ, r scales with $\mathrm{L}^{1/2}$. Equation 3.1 expresses the same scaling relation, for the inner edge of the torus. Here, r is the distance of the ionising source from the absorbing gas. From this I can infer that if warm absorbers originate at the inner edge of the torus then they should possess similar values of the product of ionisation parameter and density, independent of their ionising

luminosities.

I re-write Equation 3.1 as $R_{\rm torus} \sim K\sqrt{L}$ with $K = 3{\times}10^{-4}$. Then re-arranging Equation 3.3 ($L = \frac{\xi N_H R_l}{f}$), equating R_l to $R_{\rm torus}$, and substituting for $R_{\rm torus}$, I obtain

$$L^{1/2} \simeq \frac{\xi N_{\rm H} K}{f} \tag{4.1}$$

Taking logs of both sides then working through the algebra, I obtain

$$log\, L \simeq 2\ \log\ \xi N_{\rm H} - 2\ \log \frac{f}{K} \tag{4.2}$$

This implies a linear relationship between log L and log $\xi N_{\rm H}$ with a gradient of 2 and an intercept of $-2\ \log \frac{f}{K}$. A list of $\log N_{\rm H}$, $\log \xi$ and $\log L$ values for warm absorbers observed in 14 AGN is given in Tables 2 and 4 of B05. These authors assume a constant velocity wind in considering the energetics of warm absorbers. In Fig. 4.3, log L is plotted versus log $\xi N_{\rm H}$ for the AGN in B05 along with the parameters derived for H 0557−385 from the RGS data. We can now use Equation 4.2 to calculate the filling factor f for all the AGN in Fig. 4.3. The filling factors for all absorber phases are listed in Table 4.1.

The absorber of PG 0844+349 and one of the absorbers in PG 1211+143 would have filling factors larger than 1 if they originated at the inner edge of the torus, so they cannot originate as torus winds. Pounds et al (2003a, 2003b) and B05 argue that the absorbers in these objects originate as accretion disk winds; from Table 4.1 these must originate closer in than the torus, so the results are consistent with an accretion disk wind.

In Table 4.1 there are 5 absorbers for which I compute very low filling factors ($f < 10^{-4}$). These absorbers have the smallest values of log ξ in the sample, ranging from 0 to 0.68 (except for the absorber with log $\xi = 2$ in Ark 564). The AGN in question are H 0557−385, MR 2251-178, IRAS 13349+2438, NGC 4593, NGC 5548 and Ark 564.

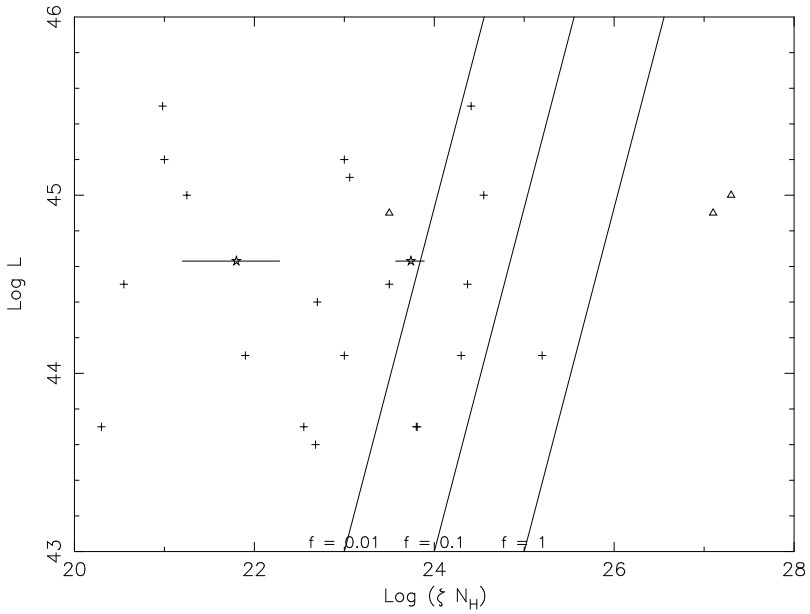

Figure 4.3: Log values of ionising luminosity, versus the log of the product of ionisation parameter and column density, for 14 AGN. H 0557−385 is shown as starred points, along with errors. Data for all other AGN are from B05. The warm absorbers in PG 0844+349 and PG 1211+143, believed to be accretion disk winds, are shown as triangles. Some different filling factors are represented as the diagonal lines and labelled at the bottom. PG 1114+445 and PG 1309+355 are not included as this Figure was limited to results from high-resolution data.

In Fig. 4.4 the filling factors for the AGN as listed in Table 4.1 are plotted, versus those found by BO5. My method for calculating filling factors compared to that of B05 has the advantage of requiring only $\log N_{\rm H}$, $\log \xi$ and $\log L$ values for warm absorbers, and no dynamical information. In contrast, the method of B05 uses the outflow velocities of the warm absorbers, and involves calculating the momentum absorbed and scattered by the warm absorber.

Unsurprisingly, Equation 4.2 assigns much larger filling factors to the accretion disk wind absorbers than B05. For the remaining objects, the absorbers with log $\xi > 0.7$ are located in a different part of Fig. 4.4 to the 5 lower-ξ absorbers, which are found on the left-hand side of the plot. The absorbers with $\log \xi > 0.7$ have $-4 < \log f < 0$ in both methods. Their mean log f from B05 is -1.8±0.2 with a standard deviation of 0.7, and their mean log f from this work is -2.1±0.2 with a standard deviation of 0.8 where the errors are 1 σ. Therefore the two methods yield consistent values for $\langle \log f \rangle$. It is worth comparing the standard devations of these results with the uncertainties inherent in the two methods. For my method I estimate the overall uncertainty on f to be approximately 0.5 dex (a sum in quadrature of 0.15 dex from L, 0.2 dex from ξ, 0.3 dex from $\rm N_H$ and 0.3 dex from K, the latter from the uncertainty in the distance of the inner edge of the torus). For the method of B05, I estimate an uncertainty on f of approximately 0.6 dex (a sum in quadrature of 0.3 dex from L, 0.2 dex from ξ and 0.5 dex from the absorbed and scattered momentum). Hence, the standard deviations on f derived from the two methods are comparable with the errors estimated for the two methods. For the absorbers with $\log \xi < 0.7$, the mean log f from my method is -5.1±0.1 and that of B05 is -2.6±0.3.

If the assumption that the absorbers originate at the inner edge of the torus is relaxed, the values of R_l that would bring the two methods into agreement can be determined, by substituting the filling factors of B05 into Equation 3.3. These values of R_l are given in column 8 of Table 4.1. Taking the standard deviations on f found from the high-ξ group of absorbers as the uncertainties inherent in

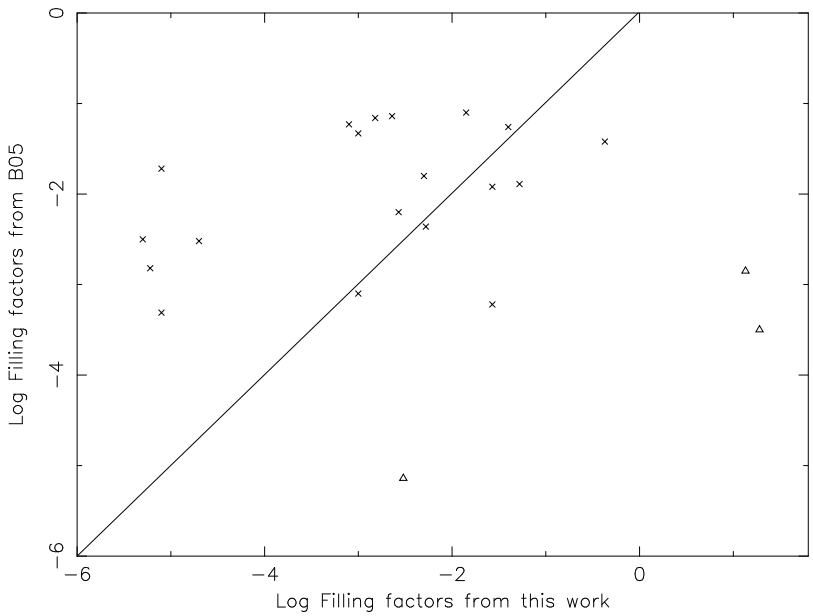

Figure 4.4: The filling factors derived from B05, which are translated from percentages into a fractional scale, plotted versus the filling factors from this work. The warm absorbers in PG 0844+349 and PG 1211+143, believed to be accretion disk winds, are shown as triangles. A line indicating equivalence between our results and those of B05 is shown.

the two methods, and summing them in quadrature, I obtain an uncertainty of $\sim$ 1 dex. This explains why some of the values of R_l determined are very large (the low-ξ absorbers in MR 2251-178 and Ark 564 are estimated to be greater than 3 Kpc distant from the nucleus). The mean of log R_l for the low-ξ absorbers is 2.63, so a typical distance for these absorbers is $\sim$ 400 pc, which is similar to the scale of the narrow-line region (Osterbrock 1993, Capetti et al 1999). At a similar distance from the continuum source, a photoionised cloud is seen in emission in X-ray observations of the prototypical Seyfert 2 galaxy NGC 1068 (Brinkman et al 2002, Ogle et al 2003). The low-ξ absorbers could be equivalent to this photoionised cloud in NGC 1068, but seen in absorption rather than in emission. It is unclear, though, whether such absorbers originate from the torus or from other, more distant, material.

Table 4.1: Comparison of volume filling factors (f) between this work, and B05. The B05 filling factors are translated from percentages into a fractional scale. 'w.a.' stands for warm absorber. R_{torus} is the distance of the inner torus edge, and R_l is the launch radius calculated for the warm absorbers using the filling factors from B05. The uncertainty on R_l is approximately ± 1 dex, see Section. 4.0.3.

AGN	Log ξ of w.a.	Log N_H of w.a.	Log L	f, this work	f, from B05	R_{torus} pc	R_l pc
H 0557−385	0.50	21.3	44.6	9×10^{-5}	—	2.0	—
	1.62	22.1		0.008	—		—
MR 2251-178	2.9	21.51	45.5	0.014	0.079	5.5	30
	0.68	20.3		5×10^{-6}	0.0031		3000
PG 0844+349	3.7	23.6	45.0	18.93	3.1×10^{-4}	3.1	5×10^{-5}
PG 1211+143	3.4	23.7	44.9	13.4	0.0014	2.7	3×10^{-4}
	1.7	21.8		0.003	7.2×10^{-6}		0.006
IRAS 13349+2438	0	21.25	45.0	2×10^{-5}	0.0030	3.1	500
NGC 4593	2.61	21.2	43.7	0.027	0.012	0.69	0.30
	0.5	19.8		8×10^{-6}	4.9×10^{-4}		40
NGC 3783	1.1	21.9	44.1	0.0027	0.0063	1.1	3
	2.3	22.0		0.053	0.013		0.3
	2.9	22.3		0.424	0.038		0.1
Mkn 509	1.76	21.3	45.1	0.001	0.047	3.4	200
NGC 7469	2.1	20.6	44.4	0.001	8.6×10^{-4}	1.5	1
NGC 3516	0.78	21.9	43.6	0.0023	0.072	0.6	20
NGC 5548	2.69	21.68	44.5	0.040	0.055	1.7	2
	1.98	21.52		0.005	0.016		5
	0.4	20.15		6×10^{-6}	0.0015		400
MCG -6-30-15	1.25	21.3	43.7	0.0015	0.069	0.69	30
	2.5	21.3		0.027	6×10^{-4}		0.02
NGC 4051	1.4	21	42.3	0.0053	0.0044	0.14	0.1
Ark 564	0	21	45.2	8×10^{-6}	0.019	3.9	10000
	2	21		8×10^{-4}	0.059		300

Chapter 5

Conclusions

For this thesis I have analysed *XMM-Newton* EPIC data of two quasars, PG 1114+445 and PG 1309+355, and EPIC and RGS data for a Seyfert 1 AGN, H 0557−385.

Compared with a sample of 23 AGN with warm absorbers studied by Blustin et al (2005), PG 1114+445 and PG 1309+355 sit at the lower luminosity end of the quasars, and H 0557−385 lies at the high luminosity end of the Seyferts.

In all three AGN I have found evidence for warm absorbers and I have studied them in detail.

The absorption in PG 1114+445 is in two phases, a 'hot' phase with a log ionisation parameter ξ of 2.57 (where ξ is in units of ergs cm s^{-1}) and a column of 5.3×10^{22} cm^{-2}, and a 'cooler' phase with log ξ of 0.83 and a column of 7.4×10^{21} cm^{-2}. An unresolved transition array (UTA) of M-shell iron is observed in the cooler phase. The absorption in this quasar is similar to that observed in the Seyfert 1 NGC 3783. I have made the first detection of warm absorption in PG 1309+355: it consists of a single phase, with log ξ of 1.87. The kinetic luminosities of these outflowing absorbers represent insignificant fractions ($< 10^{-3}$) of the energy budgets of the AGN.

For both PG 1114+445 and PG 1309+355, the absorbing gas lies at distances of 10^{19} - 10^{22} cm from the continuum radiation source, which suggests that it could originate in a wind emanating from a molecular torus.

The warm absorption in H 0557−385 can be characterised by two phases: a phase with log ionisation parameter ξ of 0.50 and a column of 0.2×10^{21} cm^{-2}, and a phase with log ξ of 1.62 and a column of 1.3×10^{22} cm^{-2}. An unresolved transition array of (M-shell) iron is detected in both phases of the absorber. For H 0557−385 I can only estimate upper limits to the distances to the absorbers, but they include the inner edge of the torus, so a torus wind is a possibility for the origin of the absorbers. From a comparison with NGC 3783 and IRAS 13349+2438, AGN with warm absorbers that also have significant UTAs similar to H 0557−385, I find that H 0557−385 is more heavily absorbed than the other two. A column of neutral gas is observed, that could originate from the AGN torus, the host galaxy disk, or a lane or cloud of gas above the disk.

UV absorption was already known to exist in PG 1114+445, and I have found good reasons to believe that the UV absorber is associated with the lower-ξ absorber. It is likely that the X-ray absorber in PG 1309+355 is associated with the UV absorber in this source too.

Finally, I have established a new method of determining the volume filling factors in warm absorbers, assuming that the ionised absorbers originate as an outflow from the torus. I derive the volume filling factors for the Blustin et al (2005) sample of AGN and compare them with those published, finding reasonable agreement, although my values are generally smaller ($\leq 1\%$) except for two quasars, thought to possess accretion disk winds. A group of five absorbers have filling factors derived in this work that are much smaller than those found by Blustin et al (2005). These absorbers all have log $\xi < 0.7$, and putting together my method with that used by Blustin et al (2005), I obtain distances for these absorbers that imply they lie out in the narrow-line region, typically hundreds of parsecs from the continuum source.

Bibliography

Antonucci R., & Miller J.S., 1985, *Astrophys. J.,* **297**, 621

Antonucci R., 1993, *Ann. Rev. Astron. Astrophys.*, 31, 473

Barvainis R., 1987, *Astrophys. J.,* **320**, 537

Bechtold J., Dobrzycki A., Wilden B., *Astrophys. J. Suppl.,* 2002, **140**, 143 (BO2)

Behar E., Sako M., Kahn S.M., 2001, *Astrophys. J.,* **563**, 497

Beichman C.A., Soifer B.T., Helou G., Chester T.J., Neugebauer G., Gillett F.C., Low F.J., 1986, *Astrophys. J.,* 308, L1

Blustin A.J., Branduardi-Raymont G., Behar E., Kaastra J.S., Kahn S.M., Page M.J., Sako M., Steenbrugge K.C., 2002, *Astr. & Astrophys.,* **392**, 453

Blustin A.J., Branduardi-Raymont G., Behar E., Kaastra J.S., Kriss G.A., Page M.J., Kahn S.M., Sako, M., et al, 2003, *Astr. & Astrophys.,* **403**, 481

Blustin A.J., Page M.J., Fuerst S.V., Branduardi-Raymont G., Ashton C.E., 2005, *Astr. & Astrophys.,* 431, 111 (B05)

Brandt W.N., Mathur S., Reynolds C.S., Elvis M., 1997, *Mon. Not. R. astr. Soc.,* **292**, 407

Brinkman A.C., Kaastra J.S., van der Meer R. L. J., Kinkhabwala A., Behar E., Kahn S.M., Paerels F.B.S., Sako M., 2002, *Astr. & Astrophys.,* **396**, 761

Brocksopp C., Starling R.L.C., Schady P., Mason K.O., Romero-Colmenero E., Puchnarewicz E.M., *in press* astro-ph/0510776

Broeils A.H., van Woerden H., 1994, *Astr &. Astrophys. Suppl.*, 107, 129

Capetti A., Axon D.J., Macchetto F.D., Marconi A., Winge C., *Mem. Soc. Astron. Ital*, 1999, 70, 41

Castor J.I.,, Abbott D.C., & Klein R.I., 1975, *Astrophys. J.,* **195**, 157

Crenshaw D.M., Kraemer S.B., Boggess A., Maran S.P., Mushotzky R.F., Wu, C., 1999, *Astrophys. J.,* **516**, 750

Crenshaw D.M., Kraemer S.B., Hutchings J.B., Bradley L.D.II., Gull T.R., Kaiser M.E., Nelson C.H., Ruiz J.R., Weistrop D., 2000, *Astr. J.,* **120**, 1731

Crenshaw D.M., Kraemer S.B., 2001, *Astrophys. J.,* 562, L29

den Herder J.W., Brinkman A.C., Kahn S.M., Branduardi-Raymont G., Thomsen K., Aarts H., Audard M., Bixler J.V., et al, 2001, *Astr. & Astrophys.,* **365**, L7

Dickey J.M., Lockman F.J., 1990, *Ann. Rev. Astron. Astrophys*, **28**, 215

Elvis M., Wilkes B.J., McDowell J.C., Green R.F., Bechtold J., Willner S.P., Oey M.S., Polomski E., et al, 1994, *Astrophys. J. Suppl.,* , 95, 1

Elvis M., 2000, *Astrophys. J.,* **545**, 63

Elvis M., 2004, AGN Physics with the Sloan Digital Sky Survey, ASP Conference Series, Volume 311. San Francisco: Astronomical Society of the Pacific, 2004, p.109

Fabian A.C., Iwasawa K., Reynolds C.S., Young A.J., 2000, PASP, 112, 1145

Fairall A.P., McHardy I.M., & Pye J.P., 1982, *Mon. Not. R. astr. Soc.,* 198, 13P

Fanaroff B.L., & Riley J.M., 1974, MNRAS, 167, 31P

Fath E.A., 1909, *Lick Observatory Bulletin 5*, **p.71**, 1909

George I.M., Nandra K., Laor A., Turner, T.J., Fiore F., Netzer H., Mushotzky R.F., 1997, *Astrophys. J.,* **491**, 508

Halpern J.P., 1984, *Astrophys. J.,* **281**, 90

Haardt F., & Maraschi L., 1991, *Astrophys. J.,* **380**, L51

Hubble E., 1926, *Astrophys. J.,* **64**, 321

Jansen F., Lumb D., Altieri B., Clavel J., Ehle M., Erd C., Gabriel C., Guainazzi M., Gondoin P., Much R., et al., 2001, *Astr. & Astrophys.,* **365**, L1

Kaastra J.S., Mewe R., Liedahl D.A., Komossa S., Brinkman A.C., 2000, *Astr. & Astrophys.,* **354**, L83

Kaastra J.S. et al., 2002, Proceedings of the Symposium on New Visions of the X-ray Universe in the XMM-Newton and Chandra Era, 26-30 November 2001, ESTEC, The Netherlands

Kallman T.R., Palmeri P., Bautista M.A., Mendoza C., & Krolik J.H., 2004, *Astrophys. J. Suppl.,* 155, 675

Kaspi S., Smith P.S., Netzer H., Maoz D., Jannuzi B.T., Giveon U., 2000, *Astrophys. J.,* **533**, 631

Kaspi S., Brandt W.N., George I.M., Netzer H., Crenshaw D.M., Gabel J.R., Hamann F.W., Kaiser M.E., Koratkar A., Kraemer S.B., et al., 2002, *Astrophys. J.,* **574**, 643

Kaspi S., 2004, Proceedings of IAU Symposium, No. 222, Cambridge University Press, 2004, p.41-4

Kinkhabwala A., Sako M., Behar E., Kahn S.M., Paerels F., Brinkman A.C., Kaastra J.S., Gu M.F., et al., 2002, *Astrophys. J.,* **575**, 732

Kirsch M. G. F., Altieri B., Chen B., Haberl F., Metcalfe L., Pollock A. M., Read A. M., Saxton R. D., et al, 2004, *SPIE*, 5488, 103

Kriss G.A., Blustin A.J., Branduardi-Raymont G., Green, R.F., Hutchings J., Kaiser M.E., 2003, *Astr. & Astrophys.,* **403**, 473

Krolik J.H, Kriss G.A., 2001, *Astrophys. J.,* **561**, 684

Krongold Y., Nicastro F., Brickhouse N.S., Elvis M., Liedahl D.A., Mathur S., 2003, *Astrophys. J.,* **597**, 832

Laor A., Fiore F., Elvis M., Wilkes B.J., McDowell J.C., 1997, *Astrophys. J.,* **477**, 93 (L97)

Laor A., 1998, *Astrophys. J.,* **505**, L83

Loaring N.S., Page M.J., Ramsay G., 2003, *Mon. Not. R. astr. Soc.,* 345, 865

Lynden-Bell, D., 1969, *Nature*, 223, 690

Magdziarz & Zdziarski, 1995, *Mon. Not. R. astr. Soc.,* **273**, 837

Maiolino R., Rieke G.H., 1995, *Astrophys. J.,* **454**, 95

Malkan M. A., Gorjian V., Tam R., 1998, *Astrophys. J. Suppl.,* 117, 25

Markowitz A., Edelson R., Vaughan S., Uttley P., George I.M., Griffiths R.E., Kaspi S., Lawrence A., McHardy I., Nandra K., et al., 2003, *Astrophys. J.,* **593**, 96

Mason K., Breeveld A., Much R., Carter M., Cordova F.A., Cropper M.S., Fordham J., Huckle H., et al, 2001, *Astr. & Astrophys.,* **365**, L36

Mathur S., Wilkes B., Elvis M., 1998, *Astrophys. J.,* **503**, L23 (M98)

Matt G., 2000, *Astr. & Astrophys.,* 355, L31

McKernan B., Yaqoob T., George I.M., Turner T.J., 2003, *Astrophys. J.,* **593**, 142

Morrison R., McCammon D., 1983, *Astrophys. J.,* **270**, 119

Netzer H., Kaspi S., Behar E., Brandt W.N., Chelouche D., George I.M., Crenshaw D.M., Gabel J.R., Hamann F.W., Kraemer S.B., et al, 2003, *Astrophys.*

J., **599**, 933

Ogle P.M., Brookings T., Canizares C.R., Lee, J.C., Marshall H.L., 2003, *Astr. & Astrophys.,* **402**, 849

Osterbrock D.E., 1993, *Astrophys. J.,* 404, 551

Page M.J., Davis S.W., Salvi N.J., 2003, *Mon. Not. R. astr. Soc.,* **343**, 1241

Pogge R.W., 1988, *Astrophys. J.,* **328**, 519

Porquet D., Reeves J.N., O'Brien P.O., Brinkmann W., 2004, *Astr. & Astrophys.,* **422**, 85 (P04)

Pounds K.A., King A.R., Page K.L., O'Brien P.T., 2003, *Mon. Not. R. astr. Soc.,* **346**, 1025 (2003a)

Pounds K.A., Reeves J.N., King A.R., Page K.L., O'Brien P.T., Turner M.J. L., 2003, *Mon. Not. R. astr. Soc.,* **345**, 705 (2003b)

Proga D., Stone J.M., & Kallman T.R., 2000, *Astrophys. J.,* **543**, 686

Quadrelli A., Malizia A., Bassani L., Malaguti G., 2003, *Astr. & Astrophys.,* 411, 77

Rafanelli P., 1985, *Astr. & Astrophys.,* 146, 17

Reeves J.N., O'Brien P.T., Ward M.J., 2003, *Astrophys. J.,* **593**, 65

Reynolds C.S., 1997, *Mon. Not. R. astr. Soc.,* **286**, 513

Rodríguez-Ardila A., Pastoriza M.G., & Donzelli C.J., 2000, *Astrophys. J. Suppl.,* 126, 63

Rokaki E., Boisson C., 1999, *Mon. Not. R. astr. Soc.,* 307, 41

Sako M., Kahn S.M., Behar E., Kaastra J.S., Brinkman A.C., Boller Th., Puchnarewicz E.M., Starling R., etal, 2001, *Astr. & Astrophys.,* **365**, L168

Schmidt M., Green, R.F., 1983, *Astrophys. J.,* **269**, 352

Seyfert K., 1943, *Astrophys. J.,* **97**, 28

Shang Z., Brotherton M.S., Green R.F., Kriss G.A., Scott J., Quijano J K., Blaes O., Hubeny I., 2005, ApJ, 619, 41

Steenbrugge K.C., Kaastra J.S., de Vries C.P., Edelson R., 2003, *Astr. & Astrophys.,* **402**, 477

Steenbrugge K.C., Kaastra J.S., Sako M., Branduardi-Raymont G., Behar E., Paerels F.B.S., Blustin A.J., Kahn S.M., 2005, *Astr. & Astrophys.,* **432**, 453

Strüder L., Briel U., Dennerl K., Hartmann R., Kendziorra E., Meidinger N., Pfeffermann E., Reppin C., et al, 2001, *Astr. & Astrophys.,* **365**, L18

Tarter C.B., Tucker W.H., Salpeter E.E., 1969, *Astrophys. J.,* **156**, 943

Turner M.J.L., Abbey A., Arnaud M., Balasini M., Barbera M., Belsole E., Bennie P.J., Bernard J.P., 2001, *Astr. & Astrophys.,* **365**, L27

Turner T.J., Netzer H., George I.M., *Astrophys. J.,* 1996, 463, 134

Vestergaard M., 2002, *Astrophys. J.,* **571**, 733

Woo J-H., Urry C.M., 2002, *Astrophys. J.,* **579**, 530